Scanning Transmission Electron Microscopy (STEM)

Binghui Ge

1 Introduction

1.1 Brief History of STEM

Although Baron Manfred von Ardenne (1938a, b) developed the first scanning transmission electron microscopy (STEM) in 1938, placing the image lens before the specimen instead of after the specimen as in the Ruska TEM design, it is just a sound idea in principle: he did not use a field emission source such that the 10 nm resolution images he achieved were too noisy. Crewe realized the necessity of using a high brightness cold field emission gun (FEG) (Crewe 1966) to achieve sufficient beam current in a small probe and a new microscope developed could produce a resolution about 0.5 nm (Crewe and Wall 1970; Crewe et al. 1970). Using molecule stained with uranium and thorium atoms samples individual atoms were first imaged by an electron microscope. Because of these contributions, Crewe is regarded to be the father of STEM.

The first so-called "Z-contrast" image (Crewe 1971) was formed from the ratio from the elastic signal collected by annular detector to the inelastic signal collected by the spectrometer, for their cross section ratio is approximately proportional to atomic number Z. But for crystalline materials, unlike the biology systems interested in Crewe group, the Crewe ratio method for Z-contrast imaging is not satisfiying because of the dominant influence of diffraction contrast. Success was achieved during imaging of catalyst particles with a high-angle annular dark field (HAADF) detector, by which thermal diffuse scattering (TDS) electrons are collected. Comparing with the Crewe ratio method, the signals give enhanced Z-contrast due to

B. Ge (✉)
Beijing, China
e-mail: bhge@iphy.ac.cn

R. Wang et al. (eds.), *Progress in Nanoscale Characterization and Manipulation*, Springer Tracts in Modern Physics 272,
https://doi.org/10.1007/978-981-13-0454-5_4

the minimum diffraction effects included. Since then, HAADF imaging becomes an essential part in the application of STEM.

Crewe's first microscope had no annular detector; it had a spectrometer to allow imaging at zero loss or at a chosen value of energy loss. He felt that the electron energy loss spectroscopy (EELS) signal held the greatest promise for high contrast (Crewe et al. 1968) since it contained much information, and it should be possible to use all the electrons that lose energy. Indeed, the common DNA bases could be easily distinguished in the low loss region of the spectrum (Crewe et al. 1971). The simultaneous detection of elastic scattering with an ADF detector and inelastic scattering with the spectrometer was a feature incorporated into their next microscope. This development leads to another important part of application for STEM ascribed to its flexibility, simultaneous collection of various analytical signals in addition to imaging, such as electron energy loss spectrum (EELS), nanobeam diffraction (NBD), X-ray energy dispersive spectrum (XEDS or EDS) and secondary electron spectroscopy (SES), and so on, as shown in Fig. 1. Especially when the condenser aberrations are corrected such that electron probe is focused to be below 0.1 nm and much larger current is delivered into nanoscale probe, not only atomic resolution EELS mapping (Kimoto et al. 2007) becomes true, but also EDS mapping (Chu et al. 2010; D'Alfonso et al. 2010) and even secondary electron imaging in STEM (Inada et al. 2010). STEM, now, has become a powerful and comprehensive analytical tool for the study of material and other related sciences.

1.2 Instrumentation

There are two types of STEM instruments commonly used by electron microscopists: dedicated scanning transmission electron microscope (DSTEM) and STEM attachment in TEM. With the advance of field-emission technology, there is no much difference nowadays between DSTEM and STEM mode in TEM using STEM attachments: high-brightness electron probe with the small size in STEM mode of TEM can be obtained as that in DSTEM. For the popularity of the STEM attachment in China, STEM mode in TEM is taken as example in this chapter. Unless stated particularly, the term STEM is used to present the STEM mode in TEM in the rest of this chapter.

A STEM microscope uses an FEG to generate high-brightness electron probes. At least two condenser lenses and an objective lens are usually used to form a small electron probe on the specimen. A condenser aperture is placed between the condenser lens and the objective lens to control the convergent angle of the incident electron probe according to the Ronchigram, which will be introduced in Sect. 3, to keep outside the electron waves with large phase variation. The size and the intensity of the high-energy electron probe can be manipulated by selecting the proper size of the condenser aperture.

In some STEM instruments, the electrons, passing through the specimen, directly reach the detector plane without the use of any post-specimen lenses. It is, however, desirable to have post-specimen lenses to offer great flexibility for effective utilizing

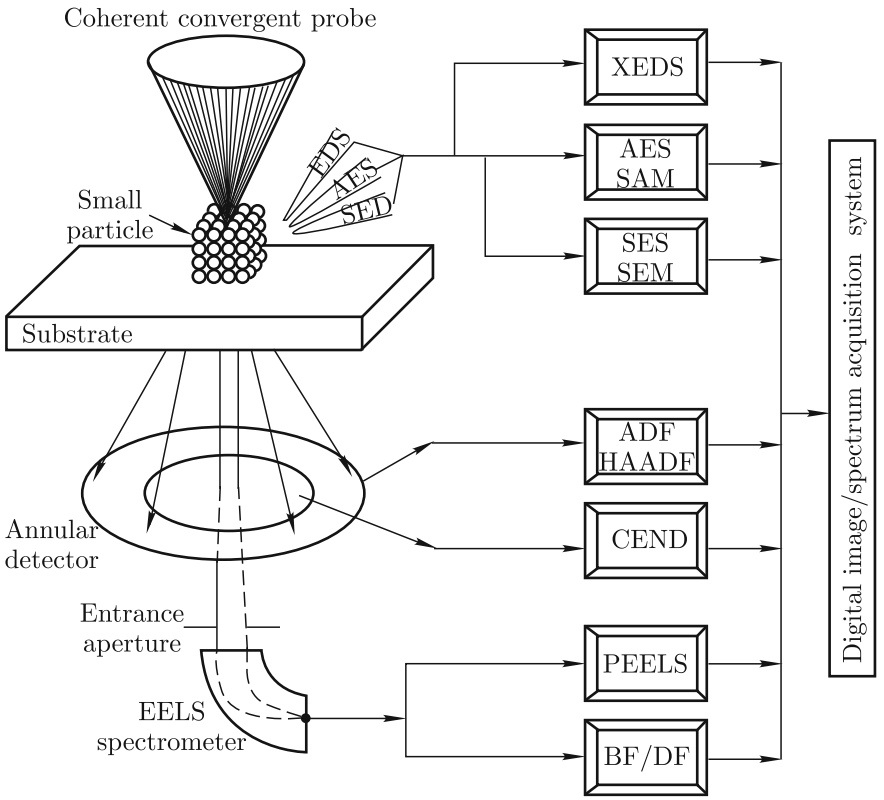

Fig. 1 Schematic diagram illustrating imaging, diffraction and spectroscopy modes commonly used in STEM: X-ray energy dispersive spectroscopy (XEDS); auger electron spectroscopy (AES) and scanning auger spectroscopy (SAM); secondary electron spectroscopy (SES) and secondary electron microscopy (SEM); annular dark-field (ADF) and high-angle annular dark-field (HAADF) microscopy; coherent electron nano-diffraction (CEND); parallel electron energy-loss spectroscopy (PEELS); and bright-field (BF) and dark-field (DF) microscopy (Liu 2000)

various detector configurations, conveniently observing and recording nanodiffraction patterns.

Interchangeable annular detectors can be installed to provide flexibility for ADF imaging or for special imaging modes using configured detectors. The attachment of a series EELS or a parallel EELS (PEELS) detectors at the bottom of the microscope column makes it possible to analyze the composition or electron structure of the sample at an atomic resolution. It also allows bright-field (BF) or dark-field (DF) imaging with only elastically scattered electrons or with other selected energy-loss electrons. A charge couple device (CCD) can be used to quantitatively record nanodiffraction patterns, shadow images or electron holograms.

For effectively collecting characteristic X-rays, a retractable, windowless XEDS spectrometer is usually attached to the column of a STEM instrument. Because of

the small volume probed by the electron nanoprobe, one or more XEDS detectors can be placed close to the sample region to increase the strength of the collected X-ray signal.

A stable operation of FEG requires the vacuum in the gun chamber to be almost 10^{-6} Pa for thermal FEG and 10^{-8} Pa for cold FEG to prevent the contamination and oxidation. While even in ultra-high vacuum, surface contamination build up on the tip of gun. Eventually, it becomes necessary to remove the contamination by "flashing" the tip for cold FEG. The column vacuum is generally better than 10^{-6} Pa to prevent significant back streaming of gas molecule into the gun chamber and to reduce the effects of contamination on the specimen surface. Most of the STEM instruments can be baked at moderate temperature for extended periods to obtain a high vacuum.

2 The Principle of Reciprocity

Before embarking on a discussion of the origins of contrast in STEM imaging, it is firstly important to consider the implications of the principle of reciprocity (Liu 2000). Consider elastic scattering so that all the electron waves in the microscope have the same energy, the propagation of the electrons is time reversible (Nellist 2011a, b). That is, the principle of reciprocity developed in the light optics can be equally applied to electron optical systems (Cowley 1969; Zeitler and Thomson 1970a, b). The wave amplitude at a point P due to a point source at Q is identical to the wave amplitude at Q due to a point source at P as shown in Fig. 2.

The essential components of a STEM imaging system are similar to those of a TEM microscope: the ray diagram of STEM is the reciprocal of that of TEM. This is demonstrated with the aid of the schematic ray diagram of Fig. 2. The STEM detector replaces the TEM electron source; the STEM gun is placed in the detector plane of the TEM; the plane of the condenser lens in TEM is used to place projector lens in STEM while the plane of projector lens in TEM to place condenser lens. Therefore, for a particular detector configuration, the contrast of STEM images can often be obtained by finding the equivalent TEM geometry. In the following, two kinds of STEM imaging, large angle BF (LABF) and annular BF (ABF) imaging, will be explained briefly by means of the principle of reciprocity.

In TEM, although the increase of illumination convergent angle destroys the phase contrast, according to the literature of Mitome et al. (1990), the point resolution of high-resolution TEM images is improved under the convergent-beam illumination (CBI) condition comparing with the parallel-beam illumination condition, because the position of first crossover of phase contrast transfer function (PCTF) shifts to the higher frequency, which means more diffraction beams transmit through the objective lens without phase reversal. According to the principle of reciprocity, the increase of the illumination convergent angle in TEM is equivalent to the increase of collection angle in STEM BF imaging. Thus, the resolution of LABF imaging will

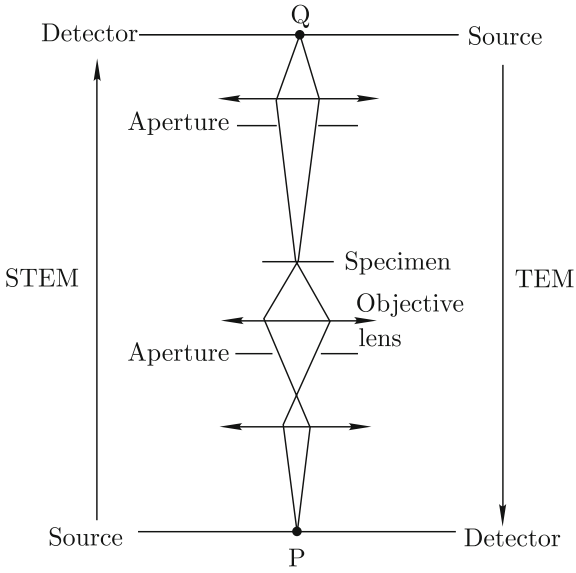

Fig. 2 Schematic ray diagram illustrating the principle of reciprocity in electron optics: the ray diagram of STEM is the reciprocal of that of TEM

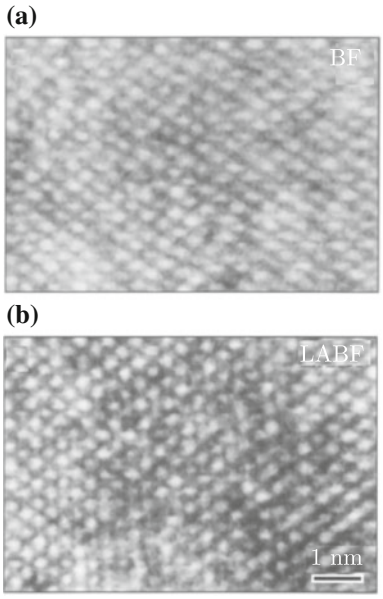

Fig. 3 Atomic resolution BF (**a**) and large-angle BF (**b**) STEM images of the same area of a GaAs crystal oriented along the [110] zone axis. The large-angle BF STEM image clearly shows a better resolution and a higher contrast (Liu 2000)

be improved comparing with BF imaging according to the results in the literature of Mitome et al. (1990). Figure 3a is a high-resolution BF STEM image of a GaAs crystal oriented in the [110] zone axis. Comparing with in BF image, a better image resolution can be seen clearly from the LABF image (semi-collection angle of about 30 mrad) with the same area as shown in Fig. 3b.

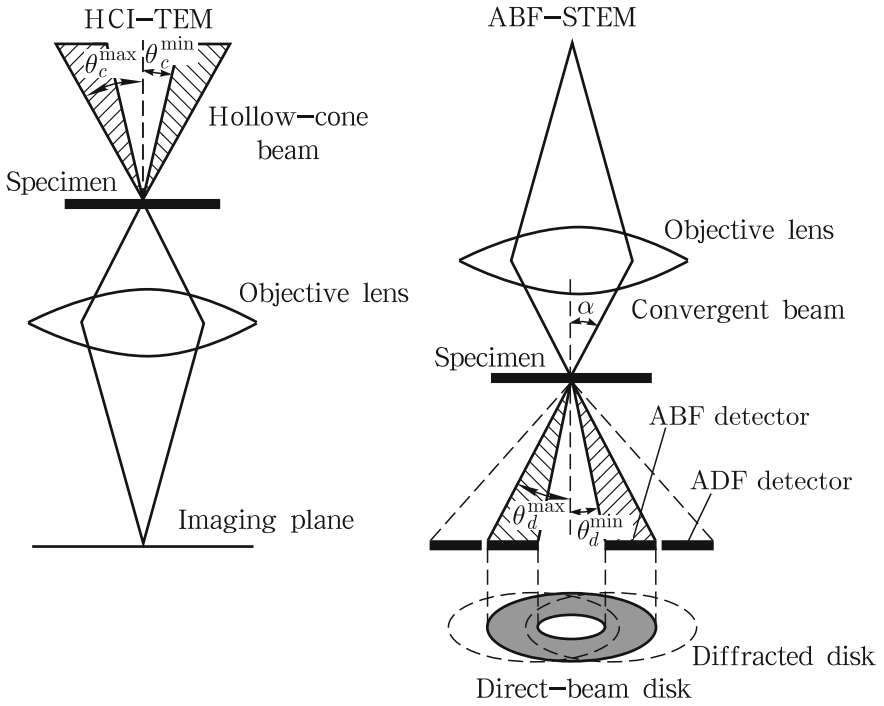

Fig. 4 Schematic ray diagrams of HCI–TEM/ABF–STEM. HCI–TEM with the cone angle ranging from minimum $\theta_c^{\min}$ to $\theta_c^{\max}$ is equivalent to ABF–STEM with the detector angle ranging from minimun $\theta_d^{\min}$ to $\theta_d^{\max}$ (Ishikawa et al. 2011)

Analogically, due to the principle of reciprocity, a recently developed imaging technique in STEM, ABF imaging (Findlay et al. 2009a, b, 2010; Okunishi et al. 2009) by locating an annular detector within the bright-field region (namely, the direct-beam disc), is equivalent to the hollow-cone illumination (HCI) imaging in TEM, which employs a series of off-axial illuminations over certain angle ranges of incident beams as shown in Fig. 4. In the early studies of optics (Mathews 1953; Hanssen 1971; Rose 1977), it was already shown as to the HCI imaging that not only the resolution is significantly improved just like that in CBI imaging, but also signal-to-noise ratio of a phase contrast due to minimizing the effect of wavelength fluctuations of the incident beam (Komoda 1966) so that ABF imaging should also have the enhanced resolution and the phase contrast, comparing with the BF imaging.

ABF imaging was first reported by Okunishi in 2009, and light atoms such as oxygen and even hydrogen (Ishikawa et al. 2011) atoms in compounds were observed. Due to this advantage combined with its insensitiveness of image contrast as to sample thickness, ABF imaging has been widely used in studying light atoms in functional materials (Gu et al. 2011). In Sect. 5, its imaging contrast theory and applications will be introduced in detail.

3 Principle of STEM Imaging

3.1 Theoretical Background

As mentioned above, the electrons was emitted from FEG and then converged by condenser lenses to form the tiny probe. After reaching the materials, the focused electrons, the probe, interact with atomic nucleus of samples and electrons outside of nucleus and they are scattered to different angles with some of them losing their energy or only changing their trajectories, depending on different scattering mechanism. Then the scattered electrons can be collected separately by different detectors through changing the camera length or detector configuration. After integration of collected electrons the intensity at one position in a STEM image is determined. When scan coils are arranged to scan the probe over the sample in a raster, a STEM image is formed.

Therefore, throughout the STEM imaging three steps can be categorized: electron probe formation, electron scattering (interaction between probe and sample), and electron collection, which will be introduced in the following.

1. Electron Probe

The full-width-half maximum (FWHM) of the probe beam is one criterion for the resolution of STEM imaging so that electron beams should be focused by condenser lenses. Meanwhile, with the reduction of the size of beam, the brightness of the beam, usually defined as the current density, will be increased, which is necessary in STEM imaging (Fultz and Howe 2008).

As to the size of the probe several factors are attributed: spherical aberration, chromatic aberration, and diffraction effect and source size.

Spherical Aberration: Spherical aberration changes the focus of off-axis rays. The further the ray deviates from the optic axis, the greater its error in focal length is. Thus, spherical aberration causes an enlargement of the image of a point. The minimum enlargement of the point is termed the "disk of least confusion." The diameter, d_s, of the disk of least confusion caused by spherical aberration is

$$d_s = 0.5 C_s \alpha_p^3 \tag{1}$$

where C_s is the spherical aberration coefficient (approximately 1 mm) for a conventional STEM, and α_p is semi angle of convergence.

Chromatic Aberration: Electrons with different energies mainly originated from the gun and specimen come to different focal points, when entering a lens along the same path. The spread in focal lengths is proportional to the spread in energy of the electrons, and it makes the image of the point a disk, too. The disk of least confusion for chromatic aberration corresponds to a diameter at the specimen, d_c

$$d_c = \alpha_p C_c \frac{\Delta E}{E} \tag{2}$$

where $\frac{\Delta E}{E}$ is the fractional variation in electron beam voltage, C_c is the chromatic aberration coefficient (approximately 1 mm).

Diffraction Effect: For an aperture that selects a range δk, the smallest spatial features in the image have the size $2\pi/\delta k$. In optics, this effect is explained as "diffraction" from the edge of an aperture. It contributes a disk of confusion of diameter corresponding to a distance at the specimen, d_d

$$d_d = \frac{0.61\lambda}{\alpha_p} \tag{3}$$

where λ is the electron wavelength. This equation is the classic Rayleigh criterion for resolution in light optics. In essence, it states that when the intensity between two point (Gaussian) sources of light reaches 0.81 of the maximum intensity of the sources, they can no longer be resolved.

Source Size: The focused spot on the specimen is, in fact, an image of the source itself, so it should be easy to form a small spot when the source itself has a small size. Assuming perfect lenses, the beam diameter, d_0, can be related with the brightness of the electron gun, β, and the convergence angle of the lens. That is,

$$d_0 = \frac{\sqrt{\frac{4I_p}{\beta}}}{\pi\alpha_p} = \frac{C_0}{\alpha_p} \tag{4}$$

where I_p is the beam current. For a given current, small values of the beam diameter are obtained by increasing the brightness (choosing a gun with higher brightness, such as FEG) or by increasing the semi angle of convergence (choosing a larger aperture, which requires a lens with smaller spherical aberration). In practice, however, α_p has a maximum value due to the lens aberrations and β is limited by the design of the electron gun such that to obtain a beam diameter with small size, only one thing can be done, sacrificing the beam current.

Taken into consideration all the contributing factors mentioned above, a general expression for the beam size, d_p, can be obtained by summing in quadrature (this is strictly valid only when all broadenings are of Gaussian shape, so that convolutions of these different beam broadenings have a Gaussian form) all diameters of the disks of least confusion from the spherical aberration, chromatic aberration, diffraction effect and source size, d_s, d_c, d_d, and d_0:

$$d_p^2 = d_s^2 + d_c^2 + d_d^2 + d_0^2 = \frac{C_0^2 + (0.61\lambda)^2}{\alpha_p^2} + 0.25C_s^2\alpha_p^6 + \left(\alpha_p C_c \frac{\Delta E}{E}\right)^2 \tag{5}$$

For a FEG, $C_0 \ll \lambda$, and the contributions of d_c and d_0 can be neglected. Superposition of the remaining terms, d_s, and d_d, yields a minimum beam size, and the parametric plot of the minimum size versus semi angle of convergence is shown in Fig. 5. ($C_s = 1.2$ mm, $\lambda = 0.00251$ nm). Furthermore, a defocus Δf needs to be

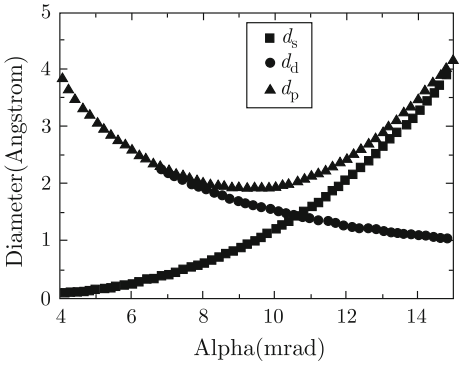

Fig. 5 Parametric plot of the minimum probe size versus semi convergence angle. $C_s = 1.2$ mm, $\lambda = 0.00251$ nm. The optimum semi convergence angle is about 9.3 mrad

chosen, similar to the Scherzer focus in HRTEM. Crewe and Salzman (1982) solved this problem, and derived that for an optimum defocus Δf_{opt} and for an optimum illumination semi-angle α_{opt}

$$\Delta f_{opt} = -(C_s \lambda)^{1/2} \tag{6}$$

$$\alpha_{opt} = (4\lambda / C_s)^{1/4} \tag{7}$$

under which the resolution limit is defined as

$$d_{min} = \frac{0.61\lambda}{\alpha_{opt}} = 0.43 C_s^{1/4} \lambda^{3/4} \tag{8}$$

which is more than 30% smaller than the Scherzer resolution for coherent imaging in high-resolution transmission electron microscopy (HRTEM).

Actually, the above considerations about the lateral size of an electron probe have clear limits (Erni 2010). The effects of diffraction, the spherical and chromatic aberrations and the infinite size of the gun cannot be treated independently. They are highly interrelated, which, in particular, becomes apparent if the electron probe is not solely considered as a two-dimensional focused electron spot but as a three dimensional entity, which, apart from the lateral extension, also has a longitudinal or vertical component. Nonetheless, the simplifications upon which they are based allow us to develop an understanding of the individual components that influence the spatial resolution in STEM imaging. In order to understand the electron probe as the result of the collective effect of all four factors mentioned above, the electron probe need to be described on the basis of wave optics rather than on purely geometrical grounds, which is beyond the scope of this chapter. However, it is important to note that the above considerations about the individual contributions to the STEM probe and their dependence on the illumination semi-angle qualitatively remain valid. For instance, it is still the spherical aberration and the diffraction limit that define the optimum STEM probe of a conventional scanning transmission electron microscope.

2. Electron Scattering and Collection

When a fine focused electron probe interacts with the specimen, the high-energy incident electrons are scattered to the different angle. Through collectors with different collection angle or different configures, different imaging contrast can be obtained corresponding to different modes, such as BF, ABF and ADF etc. (Pennycook 2011).

An electron diffraction pattern consisting of a set of convergent beam discs can be obtained when a thin crystal is oriented along a principal zone axis. If a circular STEM detector is positioned in the transmission disc, the obtained STEM image after the probe scanning over the sample is a BF image. According to the principle of reciprocity mentioned in Sect. 2, the BF imaging is similar with HRTEM coherent imaging, and its contrast is sensitive to the sample thickness and the defocus values.

Instead of the circular detector, if an annular detector is chosen to collect the electrons in the transmission disc, ABF images will be obtained. Comparing with BF images, ABF images are also sensitive to the defocus value, the feature of coherent imaging, but not to the sample thickness, which will be specifically introduced in Sect. 5. Still using the annular detector, if we decrease the camera length so that electrons of the transmission disc are excluded, ADF images are obtained. In the case of HAADF imaging with inner collection angle at least more than 50 mrad, the image contrast is insensitive to both the sample thickness and the defocus value but mainly dependent on the atomic number, Z, which is mainly ascribed to the incoherent TDS electrons. HAADF imaging, therefore, is also named Z (atomic number) contrast imaging, which will be introduced in Sect. 4. In the next, the modes of BF imaging (coherent imaging) and ADF imaging (incoherent imaging in some cases) are selected as examples to briefly explain their imaging contrast.

The amplitude distribution of the incident electrons at the exit surface of the sample can be described by a wave function $\Psi(K)$, which is the Fourier transformation of the object wave function $\varphi(R)$ multiplied by the phase factor due to the aberration of condenser lens

$$\Psi(K) = F^{-1}(\varphi(R))e^{-i\chi(K)} \tag{9}$$

where $\chi(K)$ for an uncorrected microscope is dominated by the coefficient of spherical aberration and defocus value,

$$\chi(K) = \pi\left(\Delta f \lambda K^2 + \frac{1}{2}C_s\lambda^3 K^4\right) \tag{10}$$

After the Fourier transformation into the image plane, Eq. 9 becomes a convolution and we have

$$\psi(R) = \varphi(R) \otimes F^{-1}[e^{-i\chi(K)}] \tag{11}$$

In the TEM case, the Fourier transformation of the phase changes due to aberrations, $F^{-1}[e^{-i\chi(K)}]$, is usually called contrast transfer function. While in the STEM case, it

can be treated as the probe amplitude distribution, $p(R)$. After squaring of Eq. (11), the bright filed image intensity can be obtained as the square of a convolution

$$I_{BF}(R) = |\varphi(R) \otimes p(R)|^2 \tag{12}$$

which is the reason that bright field phase contrast images can show positive or negative contrast depending on the phase of the transfer function.

While for the imaging of a STEM annular detector, it is necessary to assume that the annular detector collects all of the scattering to convert pure phase variation to intensity variations in the ADF image (Misell et al. 1974; Engel et al. 1974). In this case we obtain the fundamental equation for incoherent imaging

$$I(R) = |\varphi(R)|^2 \otimes |p(R)|^2 \tag{13}$$

Sometimes, Eq. (13) is simplified to be

$$I(R) = O(R) \otimes P(R) \tag{14}$$

That is, the intensity of incoherent imaging is described as a convolution of an object function $O(R)$ with a STEM probe intensity profile $P(R)$ (shown in Fig. 6), and the latter also can be regarded as the point spread function. The Fourier transform of the image will therefore be a product of the Fourier transformation of the object function and the Fourier transformation of the probe intensity. The latter is known as the optical transfer function and its typical form is shown in Fig. 7 (accelerating voltage 300 kV, C_s 1 mm, defocus −44.4 nm). Unlike the phase contrast transfer function (PCTF) for BF imaging, it shows no contrast reversals and decays monotonically as a function of spatial frequency.

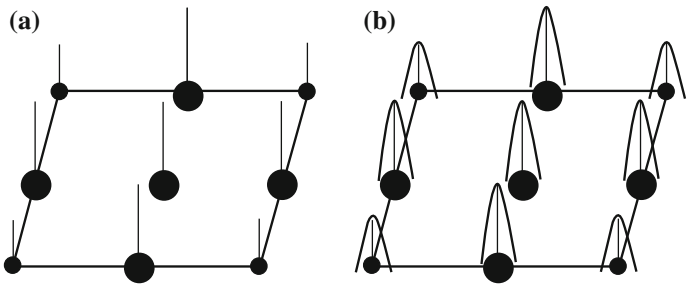

Fig. 6 **a** Ni_3Al ⟨100⟩ projected model with face-centered cubic structure and object functions represented by the weighted lines. **b** The experimental image interpreted as a convolution of the probe intensity and the object function

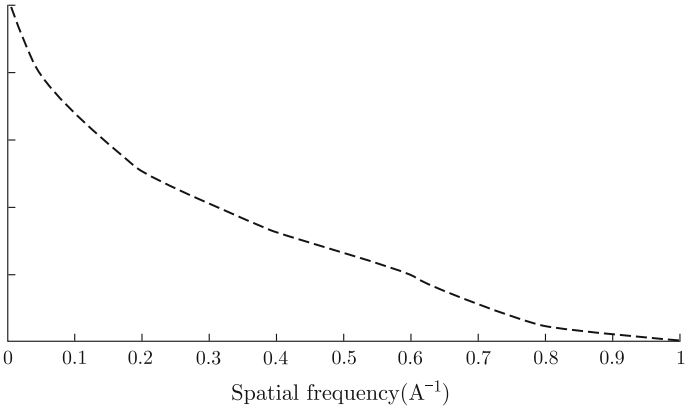

Fig. 7 A typical optical transfer function for incoherent imaging in STEM with accelerating voltage 300 kV, C_s 1 mm, defocus −44.4 nm (Nellist 2011a, b)

3.2 Ronchigram

The electron "Ronchigram" (James and Browning 1999), or "shadow image" is one of the most useful ways of characterizing and optimizing the probe. This is because the intensity, formed at the diffraction plane, varies considerably with angle, and this variation is a very sensitive function of lens aberrations and defocus (Cowley 1986). When the excitation of each illumination electron optical component is slightly changed, very small misalignments become apparent by translations in the pattern that depart from circular symmetry. Furthermore, the presence or absence of interference fringes in the pattern indicates the amount of incoherent probe broadening due to instabilities and the effect of a finite source size. Figure 8 shows schematically the ray diagram for Ronchigram formation. The probe remains stationary and the post-specimen intensity is recorded as a function of angle by a CCD camera or equivalent device.

Experimentally, to observe the Ronchigram, apertures are removed after the specimen and a large convergence angle (>100 mrad) is selected by inserting the largest condenser aperture. The Ronchigram can then be directly observed on the microscope phosphor screen or on a TV-rate CCD camera positioned beneath the phosphor screen. Camera length and positioning are controlled with the projector lenses and shift coils.

Typical Ronchigrams at the amorphous edge of a specimen are shown in Fig. 9. At large defocus as in Fig. 9a and d, the electron cross-over is at a relatively large distance from the specimen, along the optic axis, and a projection image is observed. Due to the opposite sign of defocus values, the projection images in Fig. 9a and d are reversed: the sample is at the top right in (a) but at the bottom left in (d). As Gaussian focus is approached, an angular dependence to the magnification emerges as shown in Fig. 9c, due to lens aberrations and the manner in which they change the phase of the

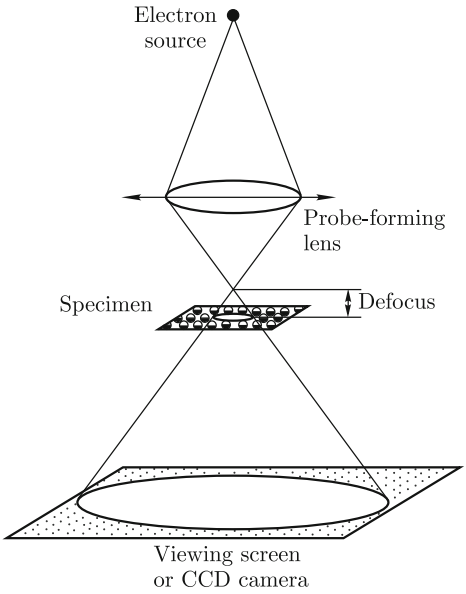

Fig. 8 A ray diagram showing formation of an electron Ronchigram (James and Browning 1999)

electron beam. At slight underfocus (see Fig. 9b), the azimuthal and radial circles of infinite magnification can be seen. These are the angles at which defocus and spherical aberration effectively cancel and they are characteristic of Ronchigrams from a round, probe-forming lens. Axial astigmatism can be very accurately corrected by exciting the stigmator coils so that these Ronchigram features are circularly symmetric. As the beam is focused, the central, low angles display the highest magnification. The coma free axis is clearly defined by this position and all alignment and positioning of detectors and apertures can be performed with respect to this spot.

The prime advantage of using a Ronchigram is that the coma-free axis is directly visible. In other alignment methods, the current or voltage center of the objective lens must be used as the reference and this is not always sufficiently accurate. Next, the illumination beam alignment can be very accurately checked by wobbling first the condenser lens excitation and then the microscope high tension. If there is a misalignment of the beam between condenser and objective lenses, there will be a periodic translation of Ronchigram features as the wobbling takes place. This can be corrected using the condenser alignment coils (CTEM bright tilt) so that the features only oscillate in and out symmetrically about the coma-free axis.

The probe has now been aligned with respect to the coma-free axis. Control of its intensity distribution is now dependent on the exact illumination lens settings and the size of the STEM condenser aperture that is subsequently inserted to exclude aberrated beams at high angles. Figure 10 shows Ronchigrams from a thin region of Si ⟨110⟩ at slight defocus. Diffraction effects are clearly presented in the pattern and lattice fringes are observed if the probe coherence is great enough. It is the movement of these fringes across the relevant STEM detectors, as the probe is scanned, that gives

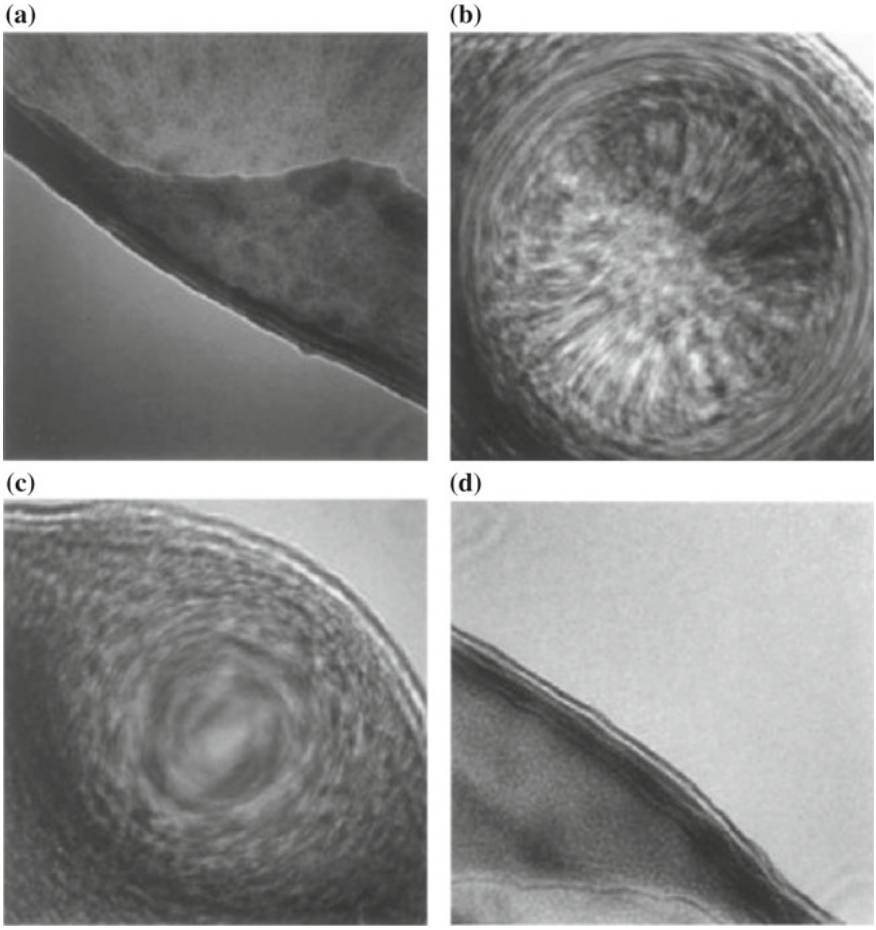

Fig. 9 Experimental electron Ronchigrams of a thin amorphous carbon layer (James and Browning 1999). **a** Large underfocus-rays at all angles cross the optic axis after the specimen and a shadow image of the specimen edge is seen. **b** Small underfocus-low angle rays cross the optic axis after the specimen. High-angle rays cross before the specimen, because of the effect of spherical aberration. The shadow image therefore changes in magnification as a function of angle and critical angles occur where there is infinite radial and azimuthal magnification. Departures from circular symmetry indicate the presence of astigmatism. **c** Gaussian focus-the lowest angle rays cross the axis at the specimen; higher angle rays cross before it, due to the effect of spherical aberration. **d** Overfocus-rays at all angles cross the axis before the specimen and a shadow image of the specimen edge is visible

rise to image contrast. At high angles in the Ronchigram, the fringes are distorted mainly because of spherical aberration of the condenser lens. This effect is lucid in Fig. 11a, a Ronchigram of silicon ⟨111⟩. Fringes correspond to the 0.192 nm {220} planar spacing. Their distortion, a function of angle from the center, is circularly

symmetric, as expected when spherical aberration is the only aberration of significance. At low angles the hexagonal arrangement of the lattice planes is more obvious from the fringe pattern. Analysis of such Ronchigrams, and derivation of electron optical parameters from them, has been carried out by Lin and Cowley (1986). Also,

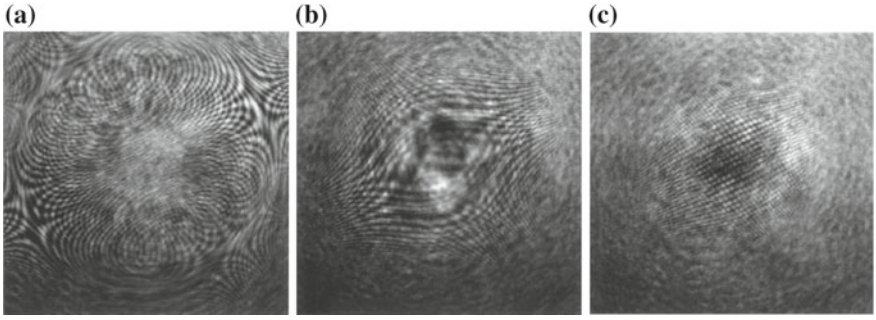

Fig. 10 Ronchigrams of a thin region of silicon ⟨110⟩ showing diffraction effects and fringes arising from the specimen periodicities (James and Browning 1999). Visibility of the characteristic fringes depends on precise tilting of the specimen and the amount of probe coherence in a direction perpendicular to the relevant crystal lattice plane. **a** Small underfocus-lattice fringes are visible near the Ronchigram center and they become heavily distorted further out in angle. The distortion is due to phase changes introduced by the lens spherical aberration. **b** Near Scherzer focus-the central fringes become large and wide. Their area corresponds to the entire overlap region between zero-order and relevant diffracted beams. **c** Slight overfocus-fringes are visible with size and spacing that decreases with increasing angle from the Ronchigram center

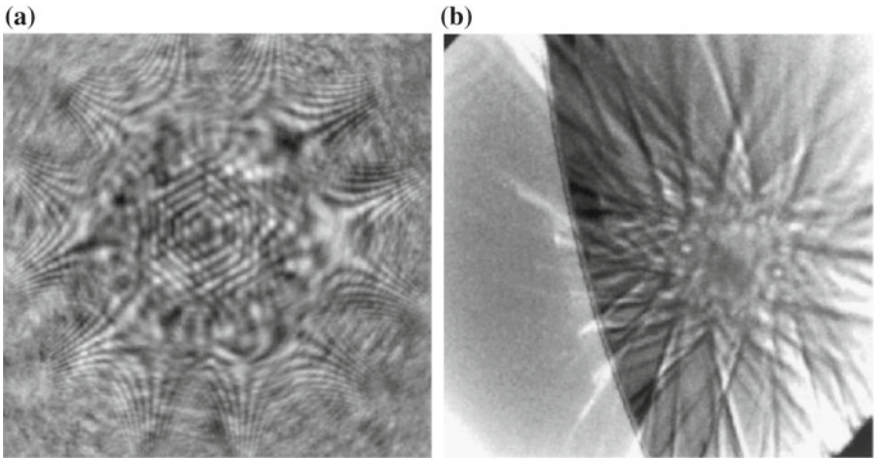

Fig. 11 **a** Ronchigram of a thin region of silicon ⟨111⟩. Interference gives rise to fringes corresponding to the 0.192 nm {220} periodicity. Spherical aberration of the probe-forming optics causes significant distortions of the hexagonal pattern away from the center. **b** Ronchigram at the edge of a silicon ⟨110⟩ crystal showing Kikuchi lines when the probe is well overfocused (James and Browning 1999)

at large defocus, when a shadow image at low magnification is visible, the crystal Kikuchi lines are seen (Fig. 11b). Since the coma-free axis position is already known, it is simple to adjust the specimen tilt so that the desired zone axis is aligned precisely for the sub-micron specimen area that is of interest.

4 HAADF Imaging

In general, HAADF imaging is thought to be mainly dependent on the accumulated atomic number of the column, being ascribed to the incoherent imaging, and contrary to high-resolution TEM imaging. Its contrast is not sensitive to small changes of defocus values and specimen thickness. In reality, however, the intensity distribution of the electron probe changes with the variation of defocus value. In crystal materials, channeling effect plays an important role in the distribution of incident electrons when transmitting along the zone axis. Thus, in some cases defocus and sample thickness as well as Debye Waller factors and other factors take an effect on the image contrast of HAADF and then HAADF imaging cannot intuitively interpreted in terms of the atomic numbers. In this section, the origin of Z dependence as to HAADF imaging will be introduced at first, and then the other influencing factors on HAADF imaging such as defocus, thickness and Debye Waller factors will be specified, respectively.

4.1 Z Dependence

1. Principle of Z-contrast imaging

According to the Theory of Bloch Waves, disruptions in the atom periodicity, including displacement disorder and chemical disorder, cause scattering of the Bloch wave states. Chemical disorder is negligible in HAADF imaging because its contribution decreases with Δk. On the other hand, diffuse scattering from displacement disorder increases with Δk as $1 - e^{-(\Delta k)^2\langle u^2\rangle}$, where $\langle u^2\rangle$ is the mean-squared displacement during thermal motion of the atoms and scales linearly with temperature, T. Differences in atomic size disorder can also make a contribution to the HAADF image, and HAADF contrast could perhaps be used to measure this type of disorder. In the present section, however, we discuss the thermal contribution to the high-angle electron scattering, thermal diffusion scattering (TDS).

When $(\Delta k)^2\langle u^2\rangle \gg 1$, the Debye–Waller factor, $e^{-(\Delta k)^2\langle u^2\rangle} \ll 1$, strongly suppresses the intensity of Bragg peaks, i.e. the coherent scattering, justifying the assumption of incoherent imaging in HAADF measurements. Even remaining some coherent scattering, after integration over a large angular range, the effects of coherence would be fatherly suppressed. Moreover, when the probe size is smaller than the spacing between aligned atomic columns in a crystal, the atom columns are illuminated sequentially as the probe is scanned over the specimen. Then each electron

is often considered as confined laterally to one atomic column (called channeling effect and to be introduced in Sect. 4.3), so the image is not affected by coherent interference between different columns. Above factors cause the HAADF imaging to be an incoherent imaging, different from the HRTEM imaging, coherent imaging.

Owing to the incoherence of the scattering, HAADF image contrast is independent of some wave interference issues involving the structure factor of the unit cell, the presence of forbidden diffractions, or some defects. The interpretation of the image is almost intuitive, that is, can be interpreted as scattering from individual atoms without phase relationships between them.

The individual atoms have their own form factors, and these must be considered when accounting for the intensity of the high-angle scattering. Combining this factor with the thermal diffuse intensity mentioned above, $1 - e^{-(\Delta k)^2\langle u^2\rangle}$, the intensity of the high-angle incoherent scattering depends on Δk as

$$\mathrm{I_{HAADF}} = |f_{\mathrm{at}}(\Delta k)|^2[1 - e^{-(\Delta k)^2\langle u^2\rangle}] \tag{15}$$

The atomic form factor for electrons, f_{at}, approaches the limit of Rutherford scattering at large Δk. In this case,

$$\mathrm{I_{HAADF}} = \frac{4Z^2}{a_0^2\Delta k^4}[1 - e^{-(\Delta k)^2\langle u^2\rangle}] \tag{16}$$

where a_0 is the Bohr radius. The thermal diffuse intensity, the factor in the square braces in Eq. (16), approaches 1 for large Δk so that

$$\mathrm{I_{HAADF}} = \frac{4Z^2}{a_0^2\Delta k^4} \tag{17}$$

For the characteristic feature of HAADF is the dependence of atomic number, Z, HAADF imaging is also called "Z-contrast imaging". In general, HAADF images are usually formed by collecting elastically scattered electrons with the inner collection angle over 50 mrad, and the HAADF image intensity is thought to be proportional to $Z^{1.7}$. Thus, as to the HAADF imaging, Eq. (14) can be rewritten, given the sample is composed of the N atoms

$$\mathrm{I_{HAADF}}(r) = \left[\sum_{i=1}^{N} Z_i^{1.7}\delta(r - r_i)\right] \otimes P(r) \tag{18}$$

Comparing with ABF imaging with its intensity roughly proportional to the $Z^{1/3}$ in some cases (to be introduced in Sect. 5), HAADF imaging is more suitable to observe heavy atoms rather than light atoms, especially surrounded by heavy atoms.

Finally, it should be mentioned that the high-angle scattering is nearly elastic. Owing to its large Δk, however, it does involve "multiphonon scattering", where energy from the high-energy electron is used to create multiple phonons

(quanta of vibrations) in the sample, so that not all of the HAADF signal is elastic in origin. Inelastic scattering can make minor contributions to the HAADF image, at least for elements of low Z, and this contribution is also incoherent.

2. Application

Similar to the high-resolution TEM imaging, high-resolution HAADF imaging can offer the crystal structure information at the atomic scale besides the compositional information. In the following, one example (Ge et al. 2012) will be shown that through a single HAADF image both compositional interfacial width and order (Ni_3Al phases)–disorder (Ni phases) interfacial width are determined at the same time in one kind of nickel based superalloy, in which interfaces play an important role in determining the mechanical properties.

Figure 12a is a typical HAADF image of the as-cast superalloy in [001] direction with the cuboidal γ' phase (Ni_3Al with the space group Pm–$3m$) precipitated in the γ matrix (Ni with the space group Fm–$3m$), and the thickness of the sample is about 30 nm determined by the relative log-ratio method on electron energy loss spectra (Egerton 2011). Analysis of EDS shows that less heavy atoms partition into the γ' phase, which makes it display with low contrast in the HAADF image, vice versa (Ge et al. 2010, 2011). Figure 12b and c are raw atomic resolution HAADF images of γ and γ' phases, respectively, with the corresponding diffractograms inset on the bottom right. Some dots with higher contrast comparing others can be observed clearly especially in Fig. 12c, which corresponds to the heavy atoms added into superalloys for solid solution hardening such as Mo, Ta, W and Re et al. According to the projected structural models inset top right (black dots represent Al atoms, white dots Ni atoms) in Fig. 12b and c, it can be concluded that heavy atoms distribute randomly in γ phases, while in γ' phases they are preferentially located in Al site, which is in agreement with the results of the atom probe tomography (Blavette et al. 2000). This kind of ordering of the distribution of heavy atoms makes the difference between the adjacent {002} planes in γ' phases, i.e., Ni planes and (50% Ni + 50% Al(or heavy atoms)) planes alternates in ⟨001⟩ direction, while in γ phases there is no obvious difference between the adjacent {002} planes, which can be used to distinguish γ and γ' phases.

Figure 13 is a raw [001] high-resolution HAADF image of interfaces, and the difference of the image contrast between γ and γ' phases is obvious. The averaged intensity profile across the interface corresponding to the area denoted by a rectangle shown in Fig. 13 is plotted Fig. 14a. The lower background intensity in the left side, γ' phases, can be observed, which origins from lower concentration of heavy atoms as mentioned above, vice versa. Thus, from Fig. 14a the transition width of chemical composition in the superalloy can be determined to be about 2.2 nm, 6 atomic {001} planes.

In Fig. 14a, an additional feature should be noted that the image intensity keeps almost constant in the right side, while it fluctuates in the left side, which is due to the alternation of Ni planes and (50% Ni + 50% Al) planes in the ordered γ' phases. To show the variety of the image intensity clearly, the intensity ratio of each atomic column to its adjacent column was made as shown in Fig. 14b. The ratio in the right

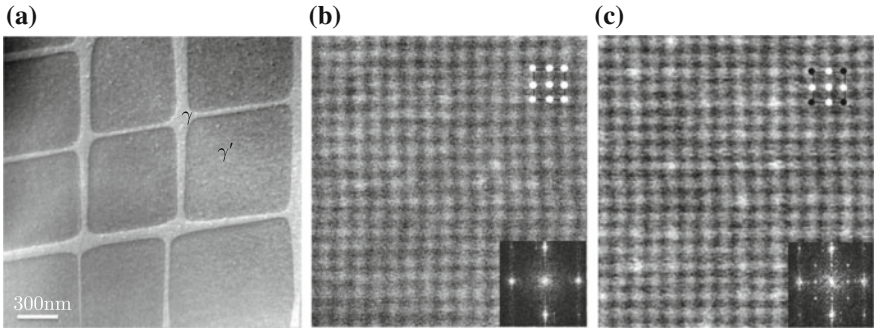

Fig. 12 **a** Low-magnification HAADF image of the superalloy and **b** and **c** high resolution HAADF images of γ and γ' phases, respectively, with their corresponding diffractograms inset on the bottom right. The projected structure models of γ and γ' are insets on the top right in (**b**) and (**c**), respectively. Black dots correspond to Al atoms and white dots Ni atoms

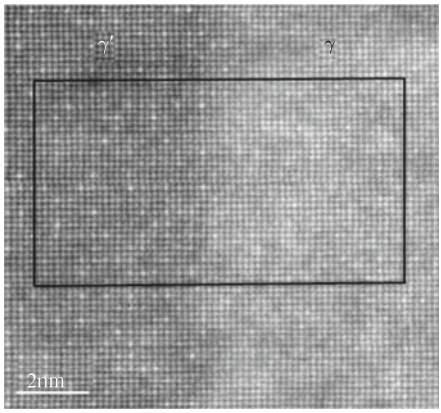

Fig. 13 Raw high-resolution HAADF image of the interface

side, the disordered γ phase, remains almost constant, i.e. 1, while in the left side, the ordered γ' phase, the ratio alternates between about 0.9 and 1.1. Thus, from Fig. 14b the interfacial width of Ni and Ni_3Al can be determined to be about 2.2 nm, same as the compositional width. Besides the equality of two kinds of interfacial width, comparing Fig. 14a with Fig. 14b, it also can be found that the transition area of the chemical composition across the interfaces of γ/γ' is exactly the same as that from the ordered phase to the disordered phase as denoted by two dotted lines.

4.2 Effect of Focus

As discussed in Sect. 1, electron probe is the Fourier transformation of the condenser lens aberration so that the probe, accurately speaking, is not like a delta function but

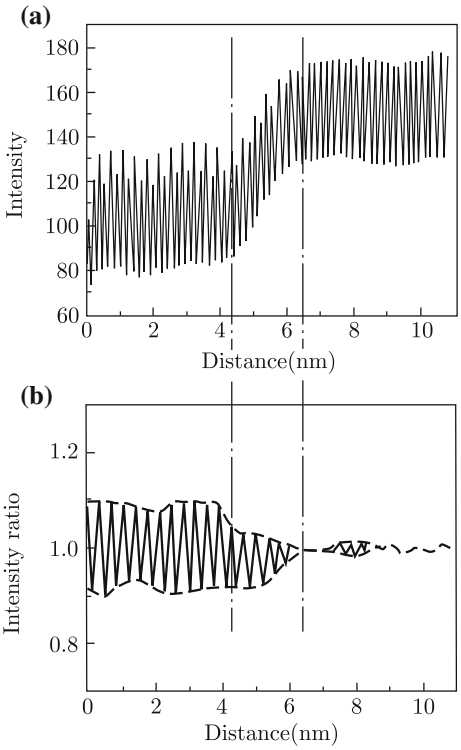

Fig. 14 **a** Averaged intensity profile across interfaces corresponding to the area denoted by a rectangle in Fig. 13 and **b** intensity ratio of each atomic column to adjacent column in (**a**)

have an intensity distribution with the subsidiary peaks symmetrically located on the side of the central peak of probe as shown in Fig. 15, the intensity profiles with series of defocus values as well as the corresponding simulated HAADF images of Si in [110] direction. From the simulated images in Fig. 15 it can be seen that image contrast changes not too much with the defocus from −500 to −900 Å, which is different from the TEM imaging, but with further deviation of defocus value the HAADF image contrast deteriorate (with defocus −300 Å) and even not reflect the structure any more (−1100 Å). This phenomenon can be interpreted by the probe intensity profiles as shown in Fig. 15 that with the variation of focus not only the FWHM of the central peak (usually defined as the resolution) changes but also the intensity of the subsidiary peaks. In the following, another example will be given that it is just due to the influence of the subsidiary peak that fictitious features could appear in the HAADF image (Pennycook et al. 1995).

Figure 16 shows the through-focal HAADF STEM images of $SrTiO_3$ in [001] direction. The intensity of oxygen columns, as highlighted by the arrowheads, seems to be enhanced in the image at $\Delta f = -70$ nm, which is above the Scherzer focus ($\Delta f = -50$ nm) of the lens ($C_s = 1.0$ mm). Both are similar with thickness 20 and 60 nm, indicating that feature in image contrast is not sensitive to the thickness (Yamazaki et al. 2001).

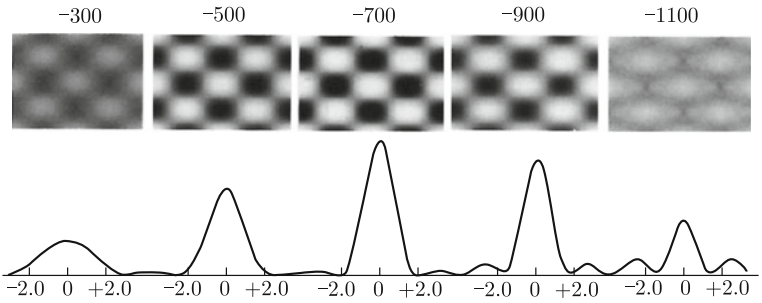

Fig. 15 Simulated defocus series for Si [110] with corresponding probe intensity profiles (100 kV, $C_s = 1.3$ mm, optimum objective aperture semiangle 10.3 mrad), giving a minimum probe size of 0.22 nm at the optimum Scherzer focus of −69.3 nm (Pennycook et al. 1995)

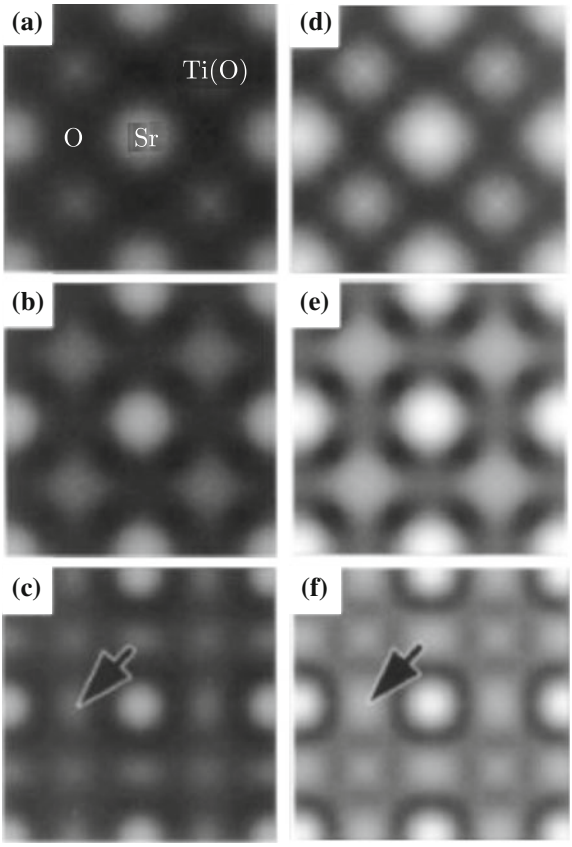

Fig. 16 HAADF image of [001] $SrTiO_3$ of 20 **a**, **b**, **c** and 60 nm thickness **d**, **e**, **f**, calculated with probes at defocus of $\Delta f = -30$, -50, -70 nm, respectively. Arrow indicates artificial spots (Yamazaki et al. 2001)

The wave fields, which are formed in the $SrTiO_3$ crystal by incident beams probed into an oxygen column (at P in Fig. 17), were calculated and shown for defocus of −50 and −70 nm in Fig. 17a and b, respectively, which disclose the intensity distribution of the wave fields along the depth (effect of sample thickness on HAADF imaging will be detailedly introduced in next section). At $\Delta f = -50$ nm, the wave packet channels almost exclusively along the oxygen columns as shown in Fig. 17a, and the subsidiary peak of the probe is weaker and does not fall into the neighboring Sr and Ti columns. Because the high-angle TDS cross section of oxygen is much lower than that of titanium and strontium, originating from the $Z^{1.7}$ dependence of HAADF imaging, there is no contrast at O columns in images shown in Fig. 16b and e. On the other hand, when the probe at $\Delta f = -70$ nm is located at the position of an O column P in Fig. 17c, its subsidiary peak coincides with the surrounding Sr columns A and B, and Ti columns C and D, as illustrated using double-headed arrow stretching between Fig. 17c and d, and the wave packet formed by the subsidiary peak channels along these Sr and Ti columns (see Fig. 17b). The HAADF detector thereby counts much TDS electrons from Sr and Ti, although the probe is located at the position of O column. Consequently, bright spots appear at the O column positions as if the O columns were visible (see Fig. 16c and f).

Above example shows the influence of focus on HAADF image contrast due to the contribution of the subsidiary peaks. Besides this, according to the imaging principle in the light optics, different focus corresponds to the different imaging plane, so with different focus the information of the different plane of sample along the beam direction can be obtained if there is a sufficient depth resolution.

In the absence of other aberrations, it is well known from the optics literature (Born and Wolf 1980) that the intensity at the center of the probe along the beam direction, z-axis, can be described as

$$I(z) = \frac{4\lambda^2}{\pi^2 z^2 \alpha^4}\left[\sin\left(\frac{\pi z \alpha^2}{2\lambda}\right)\right]^2 \tag{19}$$

where α is semi-convergent angle, so that the FWHM of the probe along the beam direction, the depth resolution, is given by

$$\delta_{\mathrm{STEM}} = \frac{1.77\lambda}{\alpha^2} \tag{20}$$

which means the depth resolution of the HAADF is inversely proportional to the square of the semi-convergent angle.

For 300 kV aberration-corrected STEM with semiangle of convergence 22 mrad, the depth resolution is about 7.3 nm (Borisevich et al. 2006) and for scanning confocal electron microscope (Nellist et al. 2008), it is further bettered by about one third, so that this kind of sectioning technique is feasible to image in three dimension. Although for conventional STEM, the sectioning technique is not practical because the semiangle of convergence is usually no more than 10 mrad (depth resolution is about 35 nm for 300 kV, C_s = 1.2 mm) due to the existence of the spherical

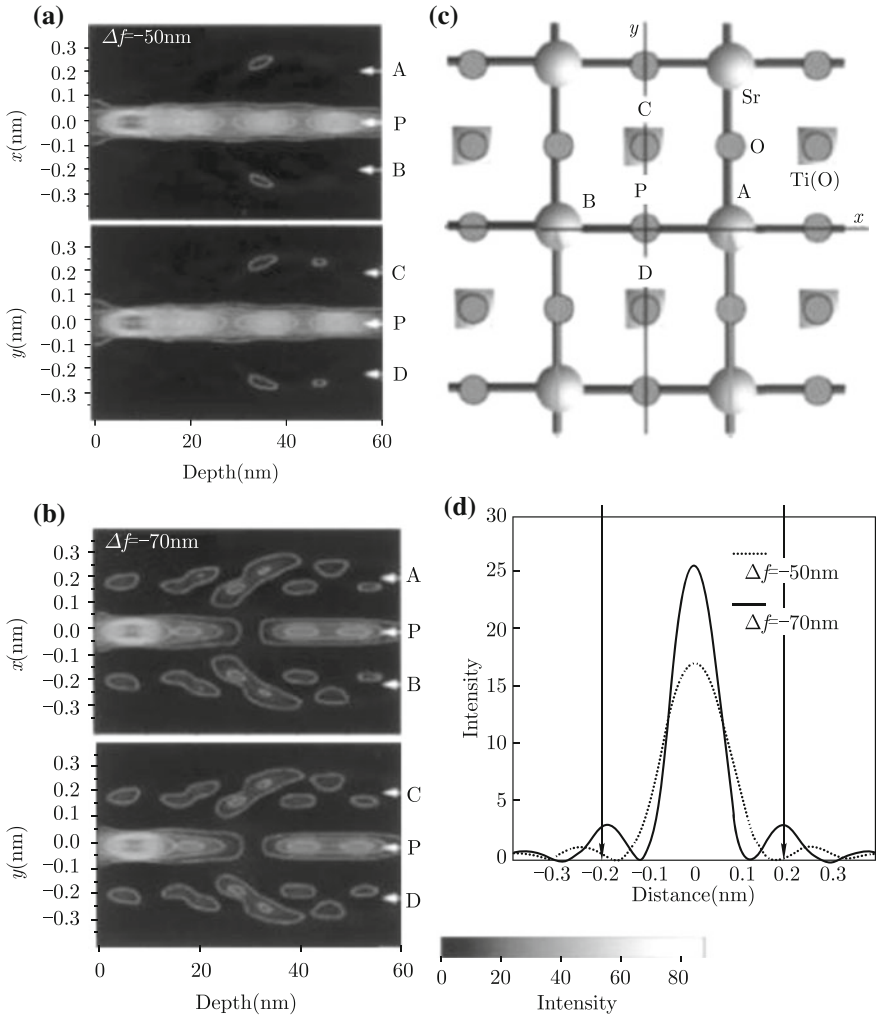

Fig. 17 **a** and **b** Intensity distribution of the wave field along the depth of A–D columns and P in [001] $SrTiO_3$, calculated for probes focus on P at $\Delta f = -50, -70$ nm, respectively. **c** Atomic column positions of the $SrTiO_3$, indicating A–D and P in (**a**) and (**b**). **d** Calculated probe functions with a semiangle of $\alpha = 12$ mrad at $\Delta f = -50, -70$ nm, respectively (Yamazaki et al. 2001)

aberration and image contrast can still be changed with different defoci. Figure 18a is a HAADF image almost under the optimum condition on some kind of crept superalloy such that the crystal lattice can be observed besides the matrix γ and precipitate γ' phases. While in Fig. 18b far from the Scherzer focus condition, the lattice fringes disappear but bright dots, heavy atom clusters, show up instead.

In all, defocus value of the condenser lens have effects on the STEM probe profile as well as the imaging plane, which will influence the contrast of HAADF image

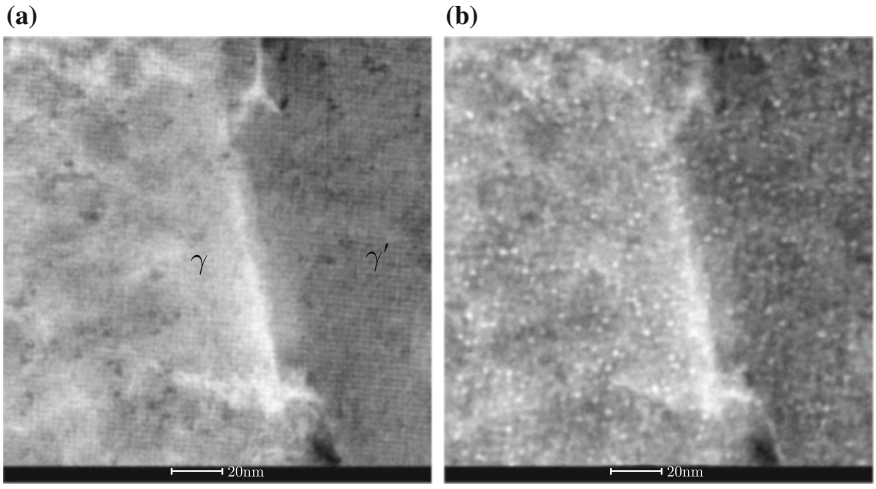

Fig. 18 HAADF images of some crept nickel superalloy with different focus value: **a** and **b** near and far from the Scherzer focus condition, respectively

like the atomic number. And due to the enhanced depth resolution of aberration-corrected STEM microscopes according to Eq. (20), more attention should be drawn to interpret image contrast.

4.3 Effect of Thickness-Channeling/Dechanneling Effect

As mentioned in Sect. 3.1, the STEM image intensity can be treated as a convolution of object function with the probe intensity profile. In that case, the entire sample is thought to be at the same focus and then the object function is convoluted with single probe intensity profile. But in reality, the intensity profile changes along the beam direction when the probe transmits through the materials, especially in the zone axis of the crystals as mentioned in Fig. 17, the probe channeling along the atomic column, which is so-called channeling effect. In this section, the influence of thickness and channeling effect are introduced at first. Then one example as to the image contrast of dopant atoms in crystals is given to show the influence of the channeling effect on HAADF image contrast. At last, some examples of dechanneling effect are shown, which is useful in the practical observation.

Considering the effect of thickness, the HAADF intensity described by the Eq. (14) should be restated mathematically. The differential contribution to the HAADF-STEM image from the layer of atoms at a depth z is simply denoted

$$\frac{dI(r,z)}{dz} = O(r,z) \otimes P(r,z) \tag{21}$$

The final image intensity $I(r)$ for a sample thickness t is

$$I(r) = \int_0^t \frac{dI(r,z)}{dz} dz = \int_0^t O(r,z) \otimes (r,z) dz \tag{22}$$

The initial probe wave function $P(r,0)$ is readily calculable usings the Fourier transformation of the condenser lens aberration. If the probe stayed in this form, it would be easy to calculate an image from Eq. (22), but that is not what happens. Instead, in a zone-axis oriented crystalline specimen, the probe strongly channels and changes along the atomic columns (Howie 1966), which, in essence, is because the atom cores present a more attractive positive potential than the interstitial regions between atoms.

A deeper explanation of channeling can be formulated by analogy to light transmission down optical fibers. Rewritten Snell's law (http://en.wikipedia.org/wiki/Snell's_law) in terms of the wavelength, λ,

$$\frac{\lambda_1}{\lambda_2} = \frac{\sin\theta_1}{\sin\theta_2} \tag{23}$$

Owing to the attractive potential of atomic nucleus the kinetic energy of electrons will be larger when electrons are close to atoms, so the wave vector in the columns of atom core is largest. That is, the wavelength of the electron in the columns of atom cores, λ_2, is shorter than the wavelength in the interstitial regions, λ_1. If the electrons fly along the direction parallel to the atomic column, the incidence angles in the atomic columns are nearly 90° as shown in Fig. 19, then the glancing angle ϕ is nearly zero. Because $\lambda_2 < \lambda_1$ in Fig. 19, from Eq. (23) $\sin\theta_2 < \sin\theta_1$. The critical condition shown in Fig. 19 has $\sin\theta_1 = 1$. In this case it is impossible for θ_2 to become larger while satisfying Snell's Law because Sin θ_1 cannot exceed 1. What happens at glancing angles shallower than the critical angle ϕ_{crit} is total reflection at the interface. That is, the electron bounces back into the column of atom cores, which leads to the channeling effect.

On the other hand, however, because crystals have a high density of atomic nuclei and electrons, the incident electrons with high probability suffer a high angle Rutherford scattering or energy loss in collision with other electrons and leave the channel. This is "dechanneling" process or "tunneling" process, which is prominent at the area with the local atomic arrangement or relaxation, such as dislocation and interface. Tunneling will be severe for the critical glancing angle ϕ_{crit}, because the electron wave function is a constant through the interstitial region and therefore appears with full amplitude in the next column of atoms. Tunneling is suppressed if the glancing angle ϕ is smaller, but it will occur even when $\phi = 0$.

Therefore, in practice, the critical angle is an important consideration in forming narrow probe beams with high-quality objective lenses. For lenses with small aberrations, larger convergent angles, α, are preferred for probe formation. A larger α allows a larger range of Δk, and hence a smaller width of the probe beam, improving lateral resolution, as well as the smaller depth of field, improving the depth

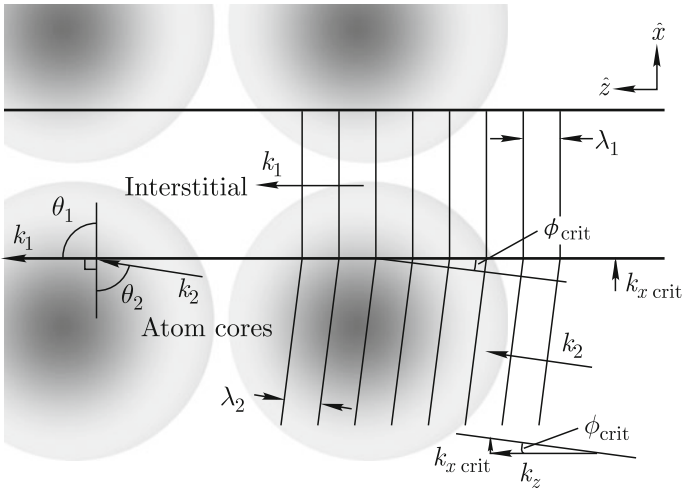

Fig. 19 Electron wave functions in a column of atoms, and in the interstitial region between atoms (Fultz and Howe 2008). The critical condition is shown, where the wave vector in the interstitial region is at 90° with respect to the interface normal

resolution (see Eq. 20). This strategy works well until α exceeds ϕ_{crit}, when only some of the electrons are channeled effectively, and many electrons are tunneled. The lateral resolution is sustained by the channeled electrons, but there is a background "noise" caused by the electrons that do not channel.

When crystals are in the zone axis and the probe channels along the column, its intensity changes quasi-periodically at the same time, which will make things complicated. In the next, it will be demonstrated by the interpretation of impurity atom contrast as an example.

At first the channeling effect was simulated as shown in Fig. 20 by means of a plane-wave multislice simulation. The initial probe produced with accelerating voltage 200 kV, C_s 1.0 mm, convergent angle 10 mrad, defocus 45.0 nm, is placed on one side of a Si ⟨110⟩ dumbbell, and we follow the probe intensity as it propagates along the atomic column. As shown in Fig. 20a, the probe quickly becomes much more intense directly on the atomic column, reaching a maximum intensity around $z = 10$ nm. The probe then dechannels somewhat, spreading intensity away from the atomic column, so that the on-column intensity is a minimum at $z = 22$ nm. The probe then rechannels, but some intensity has spread to the adjacent atomic column.

From Fig. 20 it can be seen that the HAADF image intensity of an impurity in crystals depends on its depth. For samples of thickness less than the first channeling intensity maximum, an impurity at the bottom of the sample will have higher image intensity than an impurity at the top. Therefore, if the sample is thinner than the first channeling maximum, and the likelihood of having more than one impurity in a column is small (low impurity concentration and a thin sample), we might be able to determine the depth of an impurity in the column from its image intensity.

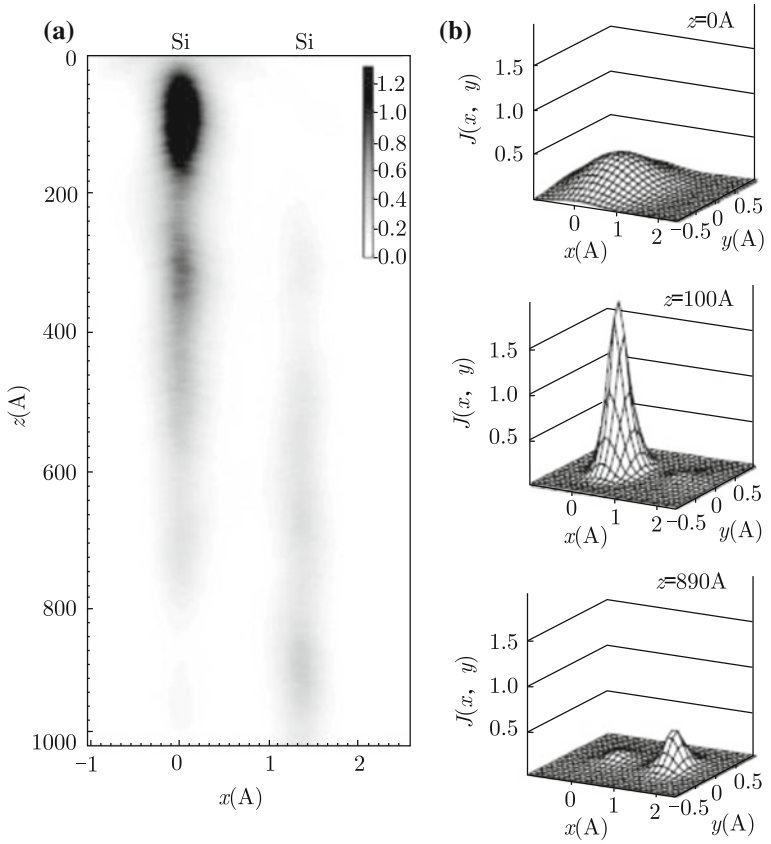

Fig. 20 **a** Grey-scale map of the probe intensity propagating down a Si ⟨110⟩ atomic column. x is position across the dumbbell, z is position along the column. The Si atomic columns are at $x = 0$ and 0.135 nm. The probe starts exactly on the left-hand side of the Si dumbbell at $x = 0$: Probe conditions are accelerating voltage 200 kV, $C_s = 1.0$ mm, 10 mrad aperture, and 45.0 nm defocus. **b** Surface plots of probe intensity versus x and y at the indicated z (Voyles et al. 2003)

If the sample is thicker than the first channeling maximum, then intensity as a function of depth is no longer single-valued and no quantitive information about the individual column occupancies or depth of impurities can be obtained from the intensity. However, if the information we seek is only the average impurity concentration (which is one of the relevant quantities for integrated circuits, for example) the channeling contribution averages out for thin samples.

At even larger thickness, we see that the probe intensity becomes greater on the neighboring atomic column than the column under that beam. The image of an impurity near the bottom of such a sample will therefore appear in the wrong atomic column. But the average dopant concentration still could be determined from such an image. These concerns emphasize the continued necessity of using thin (generally

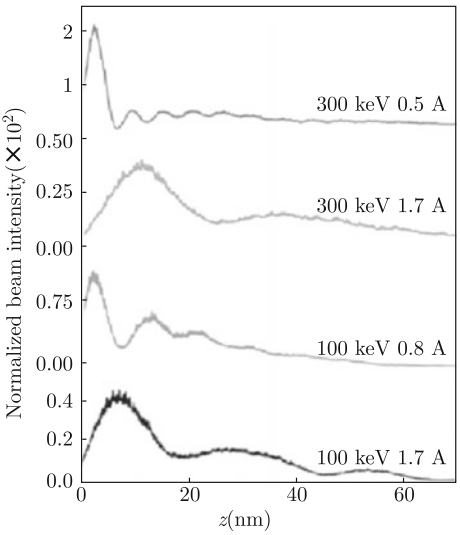

Fig. 21 Probe intensity in Si along [110] direction as the function of propagation depth (Mittal and Mkhoyan 2011). Four intensity variations are compared with different accelerating voltages and probe sizes

less than 10 nm thick) samples, even when very high spatial resolution imaging, such as with a spherical-aberration corrected STEM, is available.

It is interesting that an aberration-corrected probe should not always be the probe of choice for detection of single dopant atom inside the crystal, although the depth resolution is improved for the aberration-corrected lens as indicated by Eq. (20). From the probe intensity of Si along [110] direction as the function of propagation depth, as shown in Fig. 21, if a dopant atom is located at 4–5 nm below beam entry surface, an aberration-corrected probe will clearly have an advantage. While a dopant atom located 10 nm from the entrance surface has about higher visibility when imaged using non-corrected 0.17 nm probe instead of aberration-corrected 0.08 nm probe.

The same method can be applied to study the imaging of interstitial impurities as follows. In some structures and orientations, such as Si ⟨110⟩, an interstitial impurity may sit between the projections of the atomic columns. If the impurity is off-column, the probe wave function is not enhanced by channeling but may even be depleted. Figure 22 shows what happens to a probe placed exactly between the two atomic columns in a Si ⟨110⟩ dumbbell. For parameters same as in Fig. 20, the probe is quickly channeled onto the two adjacent columns, leaving little intensity at the initial probe positions between the columns for $z > 4$ nm. This effect is reduced with a smaller probe (Voyles et al. 2003), and significantly less evident at the actual Si interstitial position, which is farther away from any of the ⟨110⟩ atomic columns, but the general principle remains: image contrast for off-column impurities will not be enhanced due to channeling. At best the contrast will be depth independent. At worst, off-column impurities near the bottom of samples that are not very thin may be invisible. Therefore, if we want to image interstitial impurities, we could work along a zone axis that puts interstitials on-column.

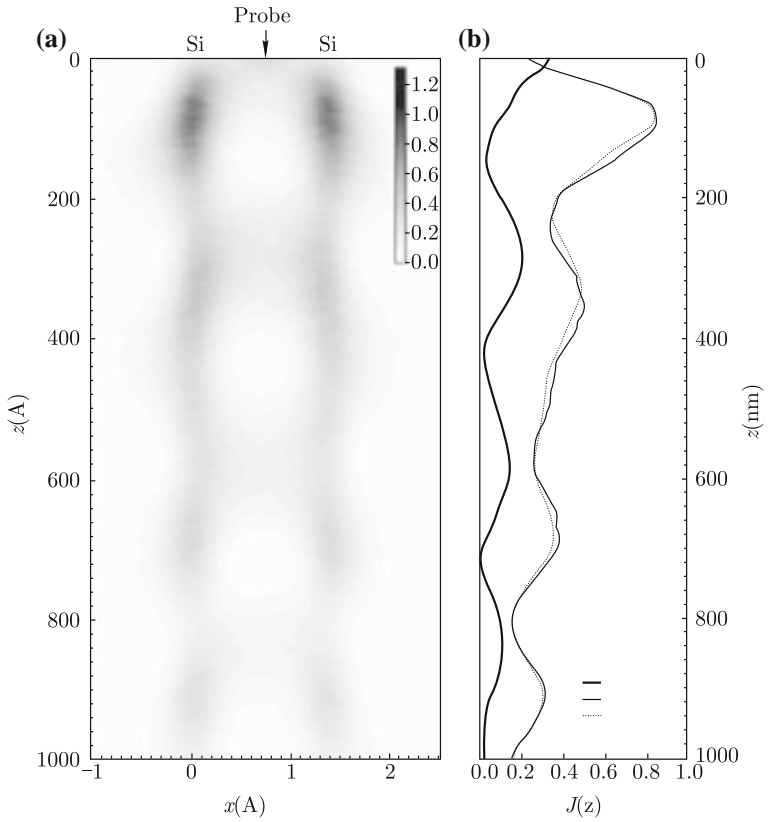

Fig. 22 **a** Grey-scale map of the probe intensity down a Si ⟨110⟩ dumbbell when the probe starts exactly between the two atomic columns at $x = 68$ pm. **b** The probe intensity within 3 pm of each atomic column, and the initial x and y position of the probe as a function of z. As in Fig. 20, the probe is strongly channeled onto the atomic columns, leaving almost no intensity below the initial probe position at $z = 14.5$ and 43 nm (Voyles et al. 2003)

On the other hand, tilting the crystals to deviate high-symmetry zone axes can avoid the strong probe channeling, which can also be used to observe interstitial impurities by HAADF imaging. Figure 23 is a tilt series of high resolution ADF images of interface between amorphous Si and crystalline Si. The column on the left is the low angle ADF (LAADF) images and the column on the right the HAADF images. From top to bottom, each pair is taken simultaneously with the sample tilted away from the [110] zone axis at an angle of 0°, 1°, 2° and 4°, respectively. Figure 23 shows that the HAADF signal decreases much faster than the LAADF signal upon tilting. The rapid decay of the HAADF signals reflects the fact that channeling electrons along aligned atomic columns contribute significantly to the HAADF images, but little to the LAADF images. Therefore, through tilting the crystals the channeling effect can be avoided and then the interstitial dopant atom can be observed by the

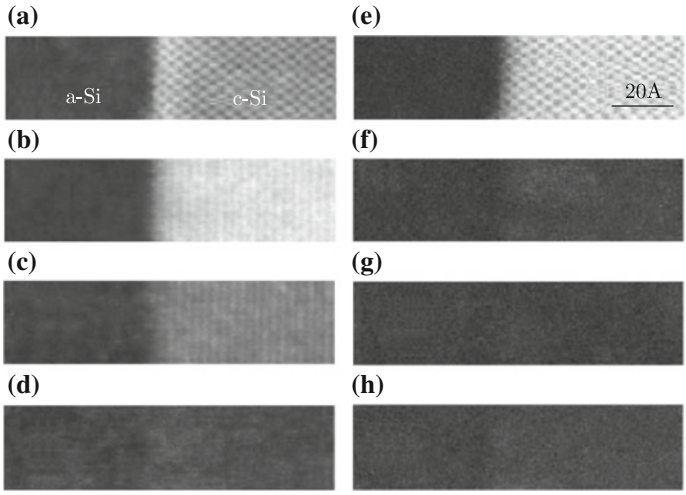

Fig. 23 High-resolution ADF images of amorphous-Si/crystalline-Si interface taken at various tilt positions (Yu et al. 2008). The column on the left is the LAADF images and the column on the right is the HAADF images. From top to the bottom, each pair is taken simultaneously with the sample tilt away from the [110] zone axis at an angle of 0°, 1°, 2° and 4°, respectively

HAADF imaging. In all, to observe the interstitial impurities two methods can be selected: to put the impurities along some atomic columns so that channeling effect works or to make the crystal deviated from the zone axis, dechanneling effect works.

Figure 23 indicates that a little deviation of zone axis will break the satisfaction of the Channeling effect. Besides this, if there exists local lattice distortion, for instance dislocation or interface, channeling effect can also break out, which will lead to abnormal contrast comparing with the bulk materials. Figure 24 shows a LAADF image and a HAADF image taken simultaneously from the interface of amorphous Si and crystalline Si (Voyles et al. 2003). There is a bright band in the LAADF

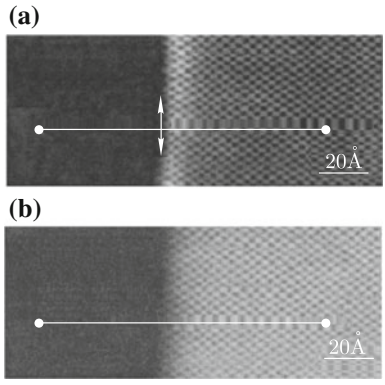

Fig. 24 Experimental ADF images of amorphous Si/crystalline Si interface taken simultaneously at ~35 nm thick by two detectors (Yu et al. 2004). **a** LAADF (20–64 mrad), **b** HAADF (64–200 mrad), The two-headed arrow indicate the location of the last visible atomic plane on the c-Si side (200 kV JEOL 2010F TEM/STEM)

image along the interface where the strain field exists, indicating a positive strain contrast. In distinction, the interface looks darker in the HAADF image, so that the contrast due to the strain field is negative in the HAADF image. Images from other regions with thicknesses above 200 Å show a similar phenomenon: positive contrast at the interface in the LAADF image and negative contrast in the HAADF image. The abnormal contrast at the interface can be understood by the dechanneling effect. Electrons which should have been scattered into high scattering angle as in the bulk materials are scattered into the low angle due to the lattice distortion of the interface, leading to the bright contrast of LAADF images and lower contrast of HAADF ones.

In a word, when electron beam transmits through the crystals it prefers piping along the atomic column, so the area along the principal axis or plane will show brighter contrast than other area in the HAADF images, while the defect such as dislocations and interfaces show darker contrast. Moreover, the intensity of electron probe, when it transmits along the zone axis, changes quasi-periodically with the different depth, so dopant atoms located with different depth may display different HAADF contrast. These two factors should be taken into consideration as to the interpretation of HAADF images.

At the end of this section, two more examples (see Fig. 25, ADF images of a certain kind of crept superalloys) are given as to the influence of STEM image contrast by channeling effect and dechanneling effect, respectively, which is useful in experiments. In Fig. 25a, a HAADF image, besides the high and striped contrast from top to bottom corresponding to the γ phases due to the partition of more heavy elements, there is octopus-shape bright contrast in the center of the image. This

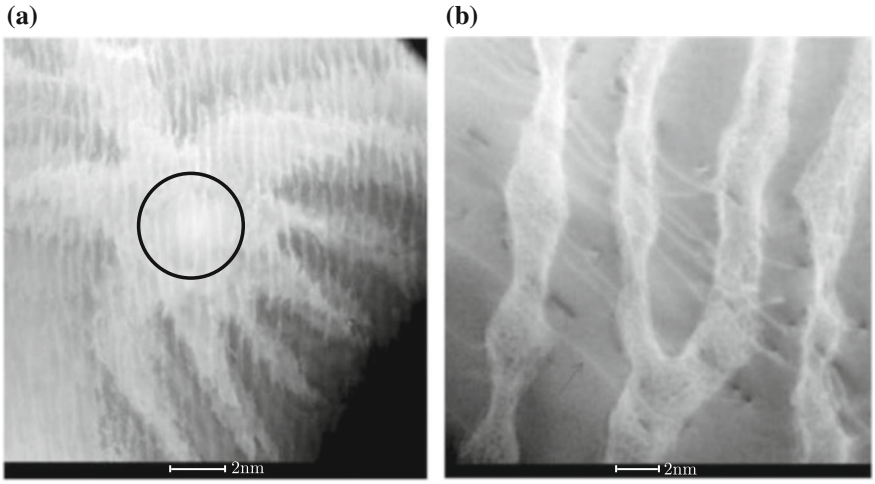

Fig. 25 Images of a certain kind of crept superalloy in **a** HAADF mode and **b** MAADF mode, respectively. The area denoted by the circle in **a** with high contrast is in the zone axis, and the white line in (**b**), one of which denoted by a red arrow, is a dislocation

abnormal contrast can be explained by channeling effect. Due to the existence of distortion in the crystal lamina only the circular area as shown in the image is in zone axis, while in the area of octopus claw some crystal plane is parallel the electron beam. This kind of image contrast is similar like the dark field (DF) diffraction contrast, which can be used for guidance of aligning of the crystals in the STEM mode. Analogously, in Fig. 25b, the medium angle ADF (MAADF) image, besides the striped contrast of γ phases, there are abnormal white contrast denoted by a red arrow, from the top left to the bottom right, which is actually originated from dislocations due to the dechanneling effect. Different with the DF imaging technique, all dislocations can be observed at the same time with bright contrast in STEM LAADF or MAADF imaging even if in the zone axis, which is useful to estimate the dislocation density of samples.

4.4 Effect of Debye-Waller Factor

According to Eq. (15), it is obvious that the HAADF image intensity is related with the Debye-Waller factor, $e^{-(\Delta k)^2\langle u^2\rangle}$. Specifically speaking, a large thermal displacement $\langle u^2\rangle$, corresponding to a small Debye-Waller factor, lead to the increase in the high-angle scattering probability and thus increase of HAADF image contrast. The effect of Debye-Waller factor in simulation has been reported recently for several different materials (Ishikawa 2002; Haruta et al. 2009; Findlay et al. 2009a, b; Blom 2012). In the experiment, Haruta et al. (2009) has observed the abnormal contrast that the contrast of Sn column appears brighter than the La columns, although the atomic number of La ($Z = 57$) is larger than that of Sn ($Z = 50$), which was interpreted by Debye-Waller factor that atom Sn with smaller Debye–Waller factor produced greater HAADF signal than atom La.

In this section, another example (LeBeau et al. 2009) will be given to show that to determine the atomic structure precisely, which is dependent on achieving the excellent agreement between the HAADF image contrast and the simulation, more factors, such as Debye Waller factor and space incoherence, should be taken into consideration besides the atomic number and thickness.

To avoid strain and nonstoichiometry, the study uses a single crystal of lead tungstate ($PbWO_4$), which contains two cations with relatively large Z($Z_{Pb} = 82$ and $Z_W = 74$). The experimentally measured Debye-Waller factors were used for the atom displacements in the frozen phonon image simulations accounting for TDS. Figure 26 shows a simulated HAADF intensity line scan along [001] across pairs of Pb and W columns with and without TDS. The term "with thermal diffuse scattering" refers to a frozen phonon calculation averaged over several configurations of the atoms (enough to obtain a reasonable convergence). By "without thermal diffuse scattering" we mean a simulation in the frozen phonon model using a single configuration with no displacements of the atoms. With TDS, the overall intensity scattered onto the HAADF detector decreases and the contrast is reduced by 19%. Both are caused by a significant decrease in the atomic column intensities due

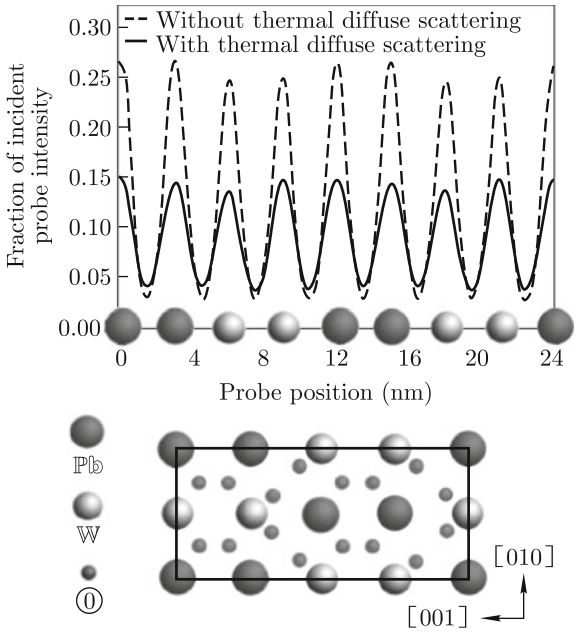

Fig. 26 (Top row) Simulated intensity line scan along [001] in a [100] projection for a 17.5-nm-thick $PbWO_4$ sample without thermal diffuse scattering (dashed line) and with thermal diffuse scattering (solid line). A [100] projection of the $PbWO_4$ is shown in the bottom row (LeBeau et al. 2009)

to thermal vibrations. Without TDS, the Pb columns would have appeared brighter than the W columns, as expected because of their larger Z. With TDS, however, the Pb and W columns have almost identical intensities. They alternate slightly in intensity (depending on the thickness) because of the different Debye-Waller factors for each column.

In addition to correctly accounting for Debye-Waller factors in the simulations, accurate measurements of the thickness are essential for comparisons between theory and experiment. In particular, strongly scattering crystals, such as $PbWO_4$, are much more sensitive to errors in the experimental thickness determination than crystals with smaller Z. Comparing with EELS, the position-averaged convergent beam electron diffraction (PACBED) patterns yield more precise and highly accurate thickness values for it is very sensitive to small changes in thickness. Although PACBED relies on comparison with pattern simulations, further validation of its accuracy comes from analyzing image intensities as a function of thickness determined by PACBED. Excellent agreement can be obtained by comparing mean HAADF image intensities in simulation and experiments as the function of thickness determined by PACBED. But the maximum atom column intensities (the intensity at which 1.5% of the total number of image pixels were above the absolute maximum image signal) still differ by a factor of 1.2–1.3 if simulations do not take into account the cumulative effects of a finite source size, sample vibration, or any other sources contributing to spatial incoherence, and a similar mismatch is observed for the background signal (the largest intensity for which 1.5% of all image pixel values fell below the absolute minimum image signal). To model the influence of spatial incoherence, the

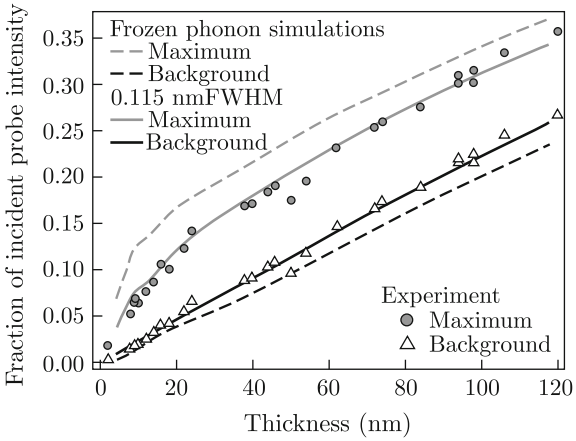

Fig. 27 Comparison of experimental (symbols) and simulated (line) image signals as a function of thickness. Both the maximum signal and minimum (background) signal are shown. The dashed and solid lines represent simulations without and with the effects of spatial incoherence taken into account by convolution with a 0.115 nm FHWM Gaussian, respectively (LeBeau et al. 2009)

simulated images were convolved with a Gaussian function (Klenov et al. 2007; Nellist and Rodenburg 1994). Figure 27 shows that after convolution with a Gaussian with a 0.115 nm FWHM, excellent agreement between experiments and simulations is obtained, and the match between experiments and simulations is within about 5% (mean error).

The above mentioned results fatherly point to potential challenges in quantitative HAADF. In particular, comparisons with simulations for crystals with heavy elements are much more sensitive to errors in foil thickness measurements than those for more weakly scattering materials. A second challenge is knowledge of the Debye-Waller factor of each atom. Although Debye-Waller factors can be measured for bulk materials, this is not the case at interfaces or near defects. A large contrast mismatch between simulations and experiments may take place due to neglecting TDS in the simulations and/or the unknown magnitude of the Debye-Waller factor in epitaxially strained films. Most importantly, because of the great sensitivity to thermal vibrations and channeling effects, image simulations are required to fully understand the image contrast, contrary to common perception that HAADF-STEM images are intuitively interpretable in terms of the atomic numbers present.

5 ABF Imaging

Light elements play key roles in a wide range of materials and devices. For example, oxygen atoms in materials critically affect the properties of oxide dielectrics, ferroelectrics, and superconductors. Much effort has been made to directly observe light

elements inside materials using TEM. But light atoms scatter electrons weakly, making them difficult to detect. Recently, Jia et al. (2005) and Jia and Urban (2004) used aberration corrected TEM with negative spherical aberration to image oxygen concentrations in complex oxides and grain boundaries, but such imaging method usually requires very thin specimens (usually <10 nm) for reliable interpretation. HAADF imaging allows direct image interpretation over a wide thickness range, but the signal scales strongly with atomic number: when heavy elements are present, light elements are barely visible. STEM EELS permits elemental analysis down to atomic level (Muller et al. 2008), but the signal-to-noise ratio is still low and detailed preprocessing is required. There remains a critical need for a real time imaging mode to robustly image light elements over a wide thickness range for materials science and device engineering applications.

A candidate technique was recently introduced by Okunishi et al. who showed images using an annular detector located within the bright field region, in which both light and heavy atom columns were simultaneously visible. By analogy to ADF imaging, this was called ABF imaging.

5.1 Basic Principle

Based on the reciprocity principle, as mentioned in Sect. 2, the ABF imaging mode could be equally realized in HCI TEM. PCTF description is used to give more fundamental, straightforward insights into why ABF-STEM is able to provide enhanced phase contrast in terms of the improved lens properties. Image formation of the phase contrast relies on a phase transfer of the scattered wave by the objective lens, which is described by the lens transfer function $-i\chi(\boldsymbol{q})$, where $\chi(\boldsymbol{q})$ is a wavefront aberration function of the scattering vector $\boldsymbol{q}$. PCTF is given as an imaginary part of the lens transfer function, and hence it results in $\chi(\boldsymbol{q})$ in the case of axial illumination. For off-axis HCI, the tilt-incident wave $\boldsymbol{K}$ as well as the scattered wave $\boldsymbol{k}$ is affected by the lens aberrations, and therefore the corresponding PCTF, $L(\boldsymbol{q})$, is written as (Rose 1974)

$$\frac{\lambda_1}{\lambda_2} = \frac{\sin\theta_1}{\sin\theta_2}$$

$$L(\boldsymbol{q}) = \int_{\theta_c}\int_{\phi} \sin(\chi(\boldsymbol{k}) - \chi(\boldsymbol{k}))d\phi d\theta_c \tag{24}$$

where ϕ represents an azimuth around the optical axis, θ_c represents a cone angle ranging from θ_c^{max} to θ_c^{min} and the scattering vector $\boldsymbol{q}$ is defined as $\boldsymbol{k} - \boldsymbol{k}$. To simplify the equation, the third-order C_s is set to be zero, and now the fifth-order spherical

aberration C_5 dominates the phase transfer of the lens. Therefore, with fixed θ_c, PCTF is given as

$$L(u, \theta_c) = \oint \sin\left[\frac{\pi}{3} C_2 \lambda^5 \{((u + \theta_c \cos\phi)^2 + (\theta_c \sin\phi)^2)^3 - \theta_c^6\}\right] d\phi \qquad (25)$$

where u presents the magnitude of $\boldsymbol{q}$, and λ is the wavelength of electrons. The HCI conditions are tuned according to Eqs. (24) and (25), and the well-optimized PCTF is obtained with 11 mrad $\leqslant \theta_c \leqslant$ 22 mrad. Information transfer now remarkably extends up to 22.5 nm^{-1}, which is far beyond from that of the typical axial illumination ($\sim$8 nm^{-1}) and corresponds to the real-space correlation length of 44.4 pm. It is noted that the entire shape of the HCI PCTF curve, like a gently sloped hill as shown in Fig. 28, may work effectively for increasing the visibility of the weak-scattering

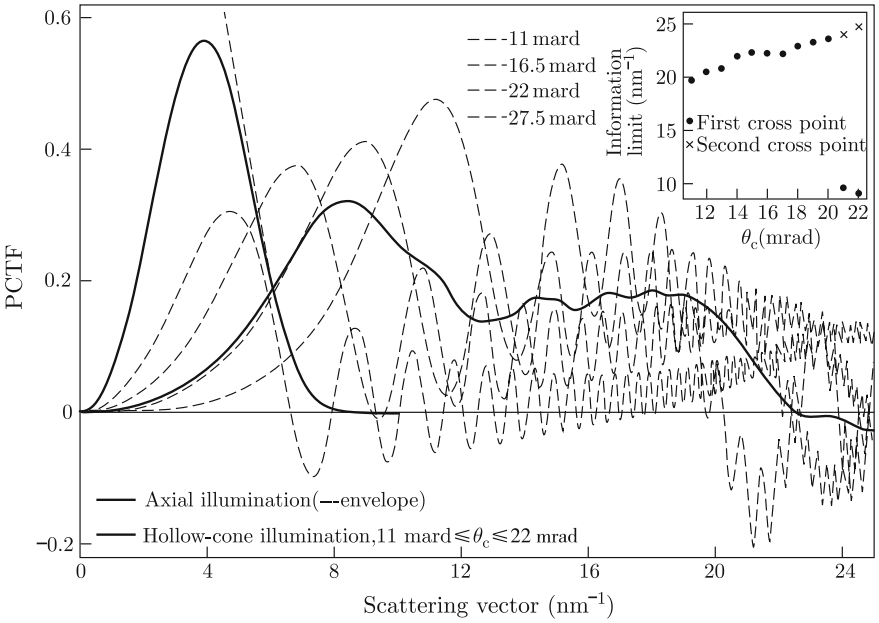

Fig. 28 HCL PCTF calculated on the basis of Eqs. (24) and (25) with $\lambda = 2.5$ pm and C_5 = 1.5 mm. Each of the dotted curves represents PCTF with the fixed θ_c Eq. (25), and its corresponding first-cross point where the curve first becomes zero (second-cross means vice versa) is plotted for each, as shown at the upper right. Note that the first-cross points occur in the low-frequency region less than 10 nm^{-1} with θ_c values larger than 20 mrad, around which the θ_c^{max} may well be optimized. The solid red curve shows the HCI PCTF integrated over $\theta_c^{min} \sim \theta_c^{max}$. PCTF with axial illumination is shown by the solid blue curve, calculated with the representative aberration-corrected TEM parameters ($C_s = -40$ μm, defocus = 9 nm, $C_c = 1.4$ mm), and the corresponding damping envelope derived with the energy spread of the beam ΔE = 0.3 eV is shown by the dashed blue line. This PCTF is shown by inverted values for comparison with the present HCI PCTF (Ishikawa et al. 2011)

light atoms, given the condition that the phases of the wave are almost equivalently transferred over wide high-frequency ranges. In the following, the basic imaging principle of ABF will be fatherly introduced with the help of image simulation. Similarities are found as to ABF imaging with HAADF imaging: Insensitivity to sample thickness and Z dependence in some cases.

Figure 29 shows an ABF and a BF defocus-thickness map for $SrTiO_3$ viewed along the [011] direction. The main feature of the ABF map is that there is a band of images centered around zero defocus and stretching out overall thickness values, in which the form of the ABF image does not change very much. Moreover, the form of these images directly represents the column arrangement of the specimen and resembles the experimental images. Thus, for suitable defocus value, ABF imaging shares with HAADF imaging the property of being relatively insensitive to specimen thickness. The range of defocus values defining this band is fairly narrow, extending from around −4 to 4 nm. The first effect of increasing the deviation of the defocus value from zero is a reduction in contrast, though as one goes further out the qualitative appearance of the images also changes.

The robustness of the visibility and interpretability of both light and heavy atom columns in the ABF image with respect to thickness is better appreciated when compared with the more usual BF images. Dramatic changes in pattern and contrast can be observed as a function of both thickness and defocus in a BF defocus-thickness map as shown in the lower panel in Fig. 29, assuming a 0–4 mrad collection angle. At zero defocus, for very thin specimens all columns, including the oxygen columns, are visible with bright contrast. For thicker specimens, the Sr columns quickly disappear. Both Ti and O columns remain bright, but the degree of brightness varies with thickness and does so at different rates for the different columns. So, for instance, for a 50 nm thick specimen at 0 nm defocus the Sr columns are dark with a faint bright halo, the O columns are perceptible only as very faint peaks, while the Ti columns are the most visible peaks. Such an image would be impossible to correctly interpret without the aid of simulations relying on the known structure.

The main reason why BF imaging is not robust with respect to thickness as ABF imaging is thought to be related with the coherent s-state interference effect and the TDS. TDS generally reduces the electron density in both the inner and outer areas of the bright field region. In the outer area of the bright field region, this reduction reinforces the reduction given by the coherent s-state interference effect-both effects combine to produce an absorptive ABF signal. However, in the inner area of the bright field region this reduction opposes the increase given by the coherent s-state interference effect—whether the contrast in a small bright field detector is positive or absorptive depends on which effect dominates for each column. We see this explicitly in the BF defocus-thickness map in the lower panel in Fig. 29: for thicknesses beyond 20 nm or so the Sr/O columns have dark contrast (TDS dominates) while the Ti and O columns have bright contrast (the s-state effect dominates), though the amount of bright contrast oscillates with thickness and does so at different rates for the different elements (because the s-state oscillations are atomic species dependent). The resulting image is visually rather confusing. Thus, coherent BF imaging is not nearly as robust with respect to thickness as ABF imaging and HAADF imaging.

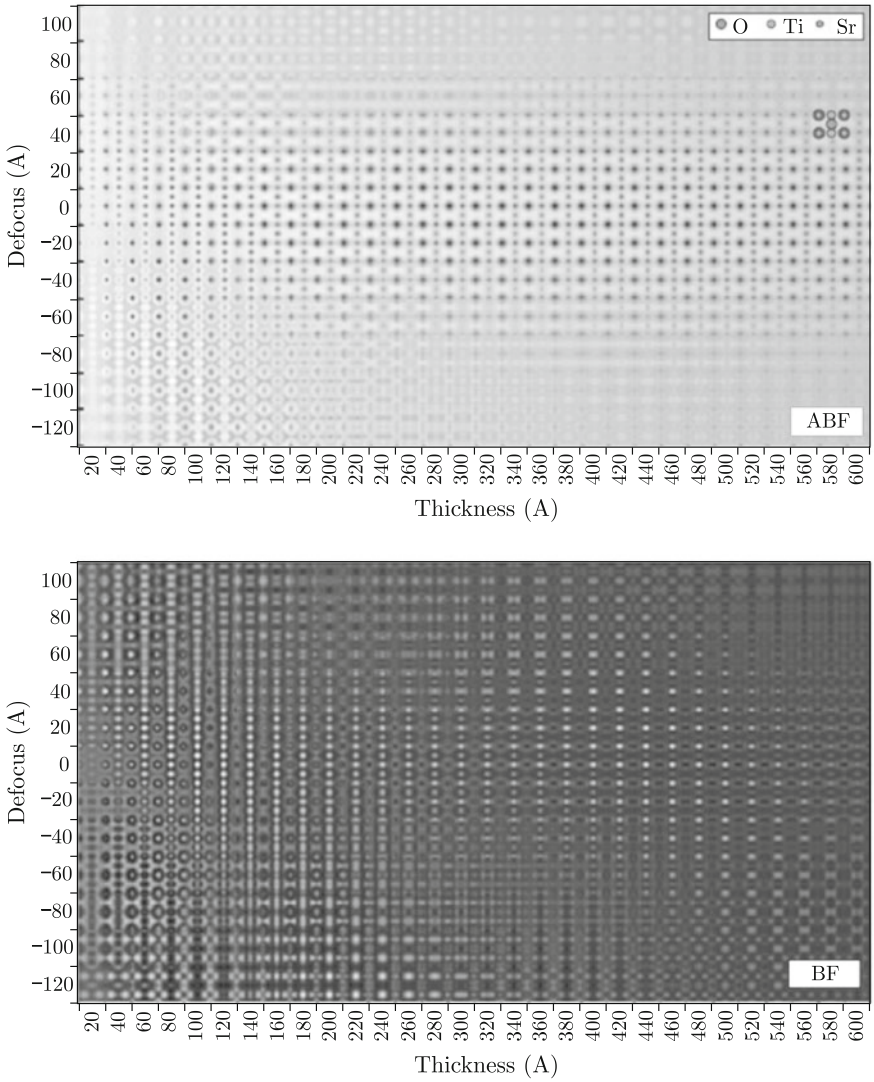

Fig. 29 Simulated defocus-thickness map for ABF (upper) and BF (lower) image of SrTiO3 viewed along the [011] orientation. The ABF images are simulated with the detector ranges 11–22 mrad, while for the BF imaging a 0–4 mrad detector was assumed. Finite source size has not been taken into account in either map (Findlay et al. 2010)

Another key feature of HAADF imaging, as mentioned in last section, is the well-known $Z^{1.7}$ scaling. In ABF imaging, in reality, some similar trend can also be observed in some cases. The on-column signal is plotted, averaged over the thickness region 30–60 nm (averaged to remove some of the remnant oscillatory behavior in this region) as a function of atomic number. It might have been expected that the role of absorption would ensure that this value decreased monotonically with increasing atomic number. This is true for the convergent angle $\alpha = 32$ mrad and $16 \leqslant \theta_c \leqslant 32$ mrad parameters as shown in Fig. 30b, but in Fig. 30a, for parameters $\alpha = 22$ mrad and $11 \leqslant \theta_c \leqslant 22$ mrad, it is seen that the signal starts to decrease with increasing Z but then increases lightly beyond $Z \approx 30$. A partial explanation for this can be found by plotting the mod-square coupling into the s-state by probe wavefunction as a function of atomic number, as shown in the dashed line on these plots. For $\alpha = 22$ mrad, it is found that at $Z \approx 30$ the coupling into the s-states reaches a maximum, and beyond this Z value decreases again.

The trend in Fig. 30b is sufficiently monotonic that we may consider approximately the Z scaling. For conceptual simplicity, rather than matching to this plot, let

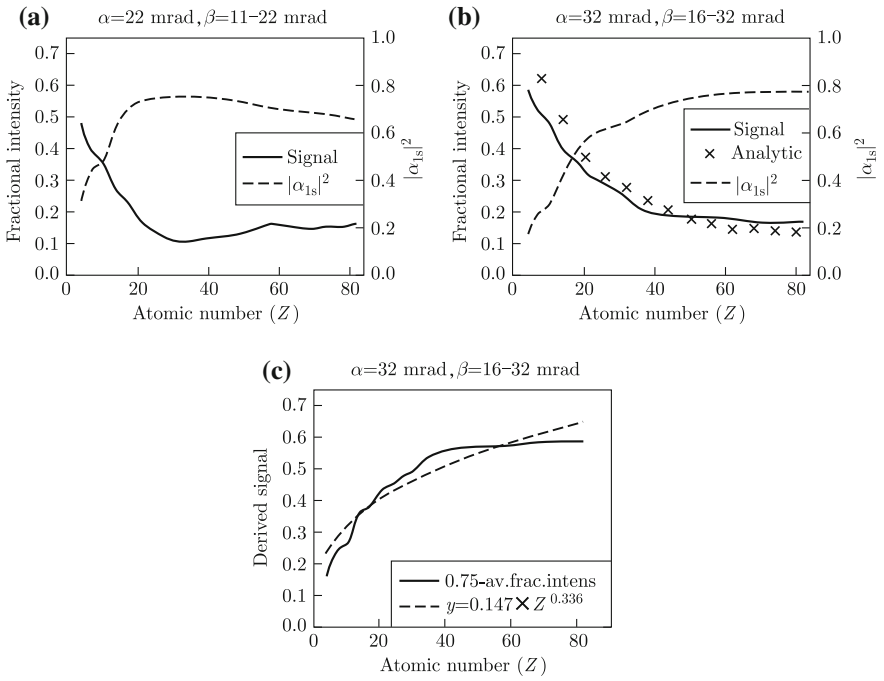

Fig. 30 Average on-column ABF signal over the thickness range 30–60 nm as a function of atomic number for **a** $\alpha = 22$ mrad and $11 \leqslant \theta_c \leqslant 22$ mrad, and **b** $\alpha = 32$ mrad and $16 \leqslant \theta_c \leqslant 32$ mrad. The right vertical axis shows the mod-square coupling amplitude to the s-state. **c** Plot of the specimen free signal (0.75) minus the averaged signal in (**b**), along with an approximate fit of this signal based on a simple parametric model (Findlay et al. 2010)

us instead consider the "signal" as the depth of the troughs relative to the specimen free limit. This produces the solid line plot in Fig. 30c, for which we can now search for a simple parametric model. Fitting to the power law relation aZ^b, it is found that $a = 0.147$ and $b = 0.336$ to give the best fit (using nonlinear least squares optimization based on the Levenberg–Marquardt algorithm, fitting to a sampling of Z in steps of 2 between 4 and 30 and in steps of 4 between 30 and 82). This is shown with the dashed plot in Fig. 30c. As a crude rule of thumb, $Z^{1/3}$ is a loosely tolerable description here, though it must be borne in mind that a fixed probe and detector aperture geometry are assumed as well as along-column spacing and Debye–Waller factor. The non-monotonic form of Fig. 30a is evidence enough that varying these parameters can change the Z-dependence. The weak Z dependence is a mixed blessing. While it is this feature which means that light and heavy atom columns are visible simultaneously, cf. the latter swamping the former as is the case in HAADF, it also means that even under ideal conditions the technique will struggle to discriminate elements of similar atomic number. For atomic species discrimination, simultaneous HAADF imaging is the more useful tool.

5.2 Other Limitation Comparing with HAADF

With smaller spacing between the columns, it is not only the "background" signal which might change in specimens. Anstis et al. (2003) have shown that the s-state channeling model, the basis for the qualitative understanding of the ABF image contrast from light columns, breaks down when the intercolumn spacing becomes small enough that the s-states of adjacent columns overlap. It will lead to an important limitation of the ABF technique: intercolumn spacing cannot reliably be measured if the columns are quite close together. It should be noted, though, that the same is true of HAADF, albeit to a smaller degree. Also, it is important to appreciate that the visibility of the contrast from either column is not significantly affected (cf. the HAADF case in which the contribution from the heavy columns due to probe spreading make it impossible to identify the light column location for the finer spacing considered here).

Another limitation of ABF indicated by the simulation is that ABF may not be a reliable tool for quantitatively assessing the degree of distortion because there is appreciable overlap for the different degrees of static displacement. While for HAADF imaging, there is greater discrimination between the signal resulting from the different degrees of static disorder, so HAADF imaging may be the better tool for trying to quantitatively assess the degree of distortion. Analogously, the fluctuation of ABF signal are found in the presence of increasing vacancies, which means that this technique is not well suited to quantifying the vacancy concentration. But because the fidelity of the HAADF signal wanes more rapidly with disorder and vacancies than the ABF signal, it is the less reliable technique for clearly detecting the presence of more distorted columns. On the contrary, robustness of ABF imaging allows us to locate the columns reliably even in the presence of a significant number of vacancies.

Another pertinent and interesting issue is the effect of specimen tilt on the form and contrast of ABF images. The ABF images are seen to be more sensitive to tilt with [011] $SrTiO_3$ as the example, with significant distortions in the form of the images by a 12 mrad ($\sim$0.69°) tilt, especially for the thicker specimen. While the HAADF images retain their qualitative form out to the same tilt, though the tilt may notably reduce the absolute signal strength.

5.3 Applications

As mentioned above, the main advantage of ABF imaging is to observe light elements, especially surrounded by heavy atoms. In this subsection, two examples will be given: firstly, the lightest element hydrogen is observed for the first time in YH_2 compound (Ishikawa et al. 2011); secondly, the ABF imaging technique is used to study the phase separation during the charging processing in $LiFePO_4$ (Gu et al. 2011), one of the most promising energy storage materials.

The YH_2 compound has a fluorite-type structure, for which the individual yttrium- and hydrogen-atom columns distinguishably appear along the [010] projection as shown in Fig. 31a. Using the ABF condition with $11 \ll \theta_c \ll 22$ mrad set up in accordance with the optimized HCI condition, the hydrogen-atom columns in a crystalline compound YH_2 was successfully imaged. Faint but distinct dark-dot contrast can be recognized at the hydrogen-atom column positions in the ABF image (Fig. 31b), the validity of which is well demonstrated by the averaged intensity profiles across the yttrium and hydrogen sites. It is noted that no significant intensity is observed at the relevant positions in the BF image (Fig. 31c) or the ADF image (Fig. 31d). It is therefore concluded that, only when the sufficiently extended PCTF is realized by HCI/ABF conditions, the hydrogen atoms can be successfully detected by phase-contrast imaging that reveals atoms as dark dots within a weak phase object (WPO) approximation. According to the log-ratio method using EELS, specimen thickness in the observed region (Fig. 31b) was estimated to be approximately 8 ± 2 nm, which is thin enough to apply a WPO approximation. Image simulations based on the multislice method are carried out with the estimated thickness of 8 nm, reproducing fairly well all the observed features, ABF, BF and ADF STEM images, as inset in each of the images of Fig. 31b–d. It is also confirmed by the simulation of ABF imaging that no significant intensity occurs at the hydrogen sites when the hydrogen atoms are removed from the structure (that is, the hypothetic fluorite YH_2 structure where all the hydrogen sites are vacant). This strongly supports the validity that the observed intensity is indeed originated from the hydrogen atoms themselves, not by the imaging artefacts of phase contrast.

Due to the great power of resolving light atoms, ABF imaging has been utilized to observe lithium element to study the working mechanism of lithium ion batteries. Here, direct observation of Li staging in partially delithiated $LiFePO_4$ is given as an example (Gu et al. 2011). In the ABF image of the pristine $LiFePO_4$ as shown in Fig. 32a, the lithium sites are in the middle of two oxygen sites, and marked by yellow

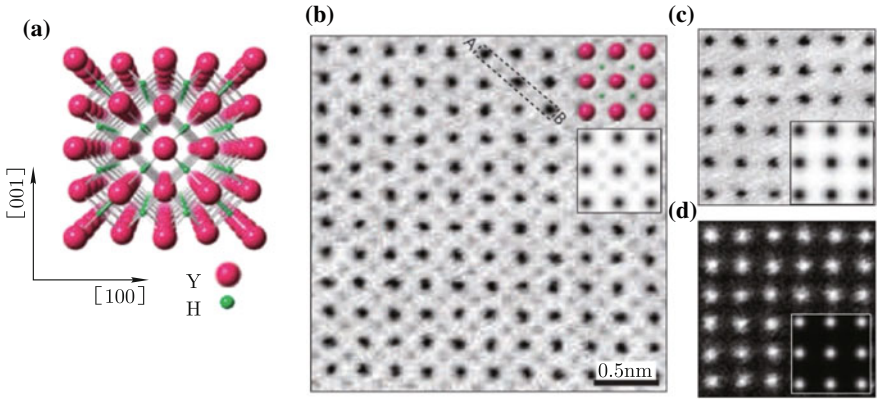

Fig. 31 ABF, BF and ADF–STEM images of the crystalline compound YH_2. **a** Crystal structure of YH_2 viewed from the [010] direction. **b–d**, ABF, BF and ADF images obtained with the detector ranges 11–22 mrad, 0–22 mrad and 70–150 mrad, respectively. Simulated images are inset in images **b–d**, and the YH_2 unit-cell projection is overlaid in (**b**) (Ishikawa et al. 2011)

circles. In the partially delithiated materials $Li_{0.5}FePO_4$ part of the lithium remains in the lattice after charging at every other row as labeled by yellow circles in Fig. 32c, and the Li extraction sites are indicated by red arrows. The high resolution atomic image shows clearly that a first order lithium staging structure exists for the partially delithiated $Li_{1-x}FePO_4$ ($x \approx 0.5$) samples, which has never been observed by other technique, and challenges previously proposed $LiFePO_4/FePO_4$ two-phase separation mechanisms. Obviously, a clear structural evolution picture of other important lithium-containing electrodes could also be disclosed now at atomic resolution based

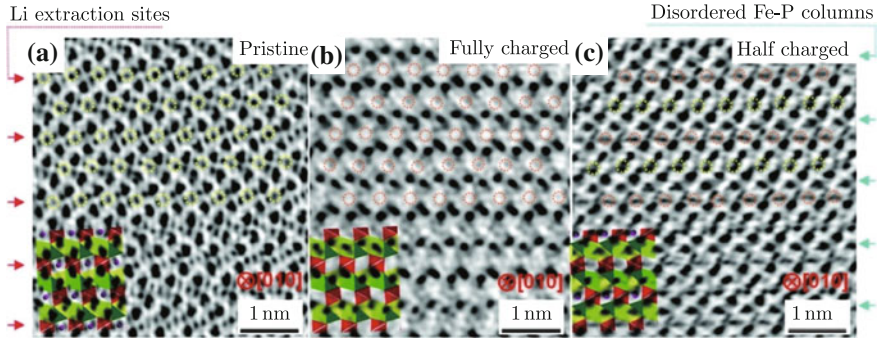

Fig. 32 ABF micrographs showing Li ions of partially delithiated $LiFePO_4$ at every other row. **a** Pristine material with the atomic structure of $LiFePO_4$ shown as inset; **b** fully charged state with the atomic structure of $FePO_4$ shown for comparison; and **c** half charged state showing the Li staging. Note that Li sites are marked by yellow circles and the delithiated sites are marked by orange circles (Gu et al. 2011)

on the ABF technique, which is indeed essential to understand Li-storage mechanisms in important energy storage materials and other materials containing small and light elements.

6 Scanning Moiré Fringe Imaging

Atomic resolution HAADF images are usually recorded at a magnification of 15 M as shown in Fig. 33a or more. From the same area, two other HAADF image were taken, Fig. 33b and c, with the magnification of 5.1 M and 1.3 M, respectively. Surprisingly, the contrast periodic in (b) is not four times as large as that in (c) but almost same as that. Undoubtedly, the lattice-like contrast of Fig. 33c is an artifact. The lattice spacing from (c) was measured to be 0.77 nm, while the real interplanar distance of this alloy should be about 0.18 nm. Detailed study at different magnifications indicates that this artifact contrast is from scanning interference between the electron beam and atomic lattice (Su and Zhu 2010). This lattice spacing was observed to be a function of the scanning spacing and the angle between the scanning and the specimen lattice, and independent of the setting of the Digital Micrograph software or the dwelling time per pixel. To distinguish this imaging method with the Moiré fringe resulting from two overlapping crystal lattices which may also appear in STEM imaging, these fringes are named as Scanning Moiré Fringes (SMF).

A geometrical model is shown in Fig. 34 to illustrate the origin of the artificial lattice. In scanning, a periodic grating lattice is created as shown in Fig. 34a. When the scan spacing (d_s) is close to the spacing of the specimen lattice (d_l), the probe would interfere periodically with arranged atom columns in the sample, as depicted in Fig. 34b. Therefore, the STEM image records the feature resulting from the interference of d_s-d_l. This process can be viewed as one wave modulated by another wave with a close frequency as a special case of frequency beating. Sinusoidal function $\sin(2\pi f x)$ is used to denote the spatial waves with frequencies f, and f_s is the spatial

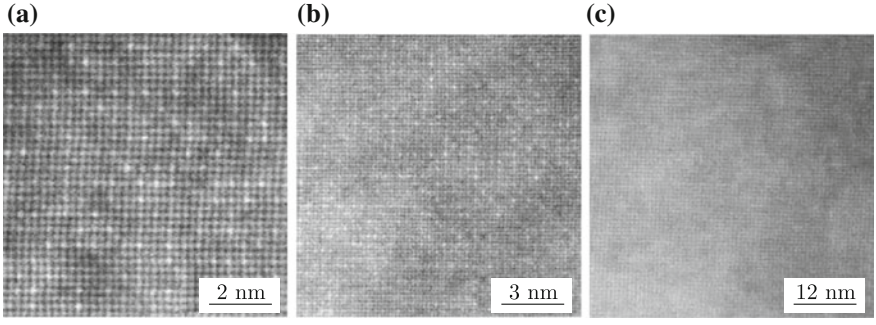

Fig. 33 **a–c** HAADF images of some superalloy along ⟨001⟩ zone axis taken with Titan 80–300 at magnifications 14.5 M, 5.1 M and 1.3 M from the same area, respectively

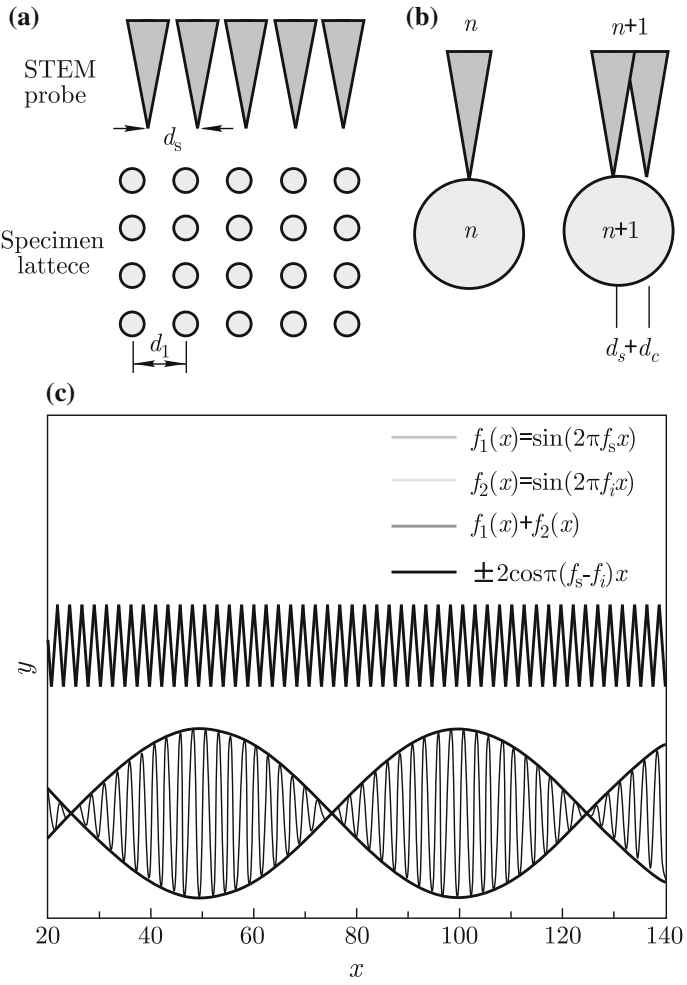

Fig. 34 Schematic diagrams showing the origin of the interference image. **a** The general view of the scanning grating and the specimen lattice. **b** The interference between neighboring scanning probes and the atomic columns. **c** The beating of two waves with frequencies f_s and f_1. Here, f_s is assumed to be 5% higher than f_1 and the amplitudes of two functions are identical (Su and Zhu 2010)

frequency of the electron probe, and f_1 is the spatial frequency of the specimen's lattice. Their sum is

$$\sin(2\pi f_s x) + \sin(2\pi f_1 x) = 2\cos\left(2\pi\frac{f_s - f_1}{2}x\right)\sin\left(2\pi\frac{f_s + f_1}{2}x\right) \qquad (26)$$

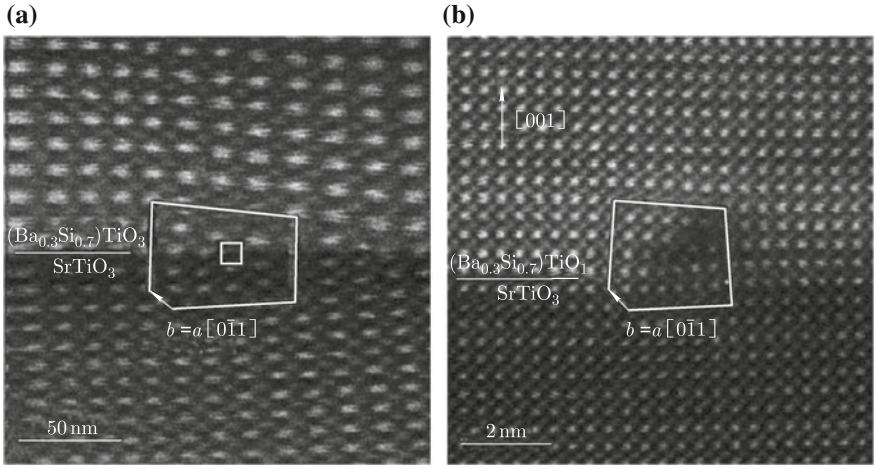

Fig. 35 **a** A SMF image at the magnification of 500 k, showing the enlarged image of a misfit dislocation at the interface of BST film and STO substrate. **b** A HAADF image taken at the magnification of 15 M on the green square region shown in (**a**), where in a Burger vector of $b = a[0\bar{1}1]$ is indicated by a Burger circuit (Su and Zhu 2010)

The beating is an envelope function of the sum, deduced as $2\cos\left(2\pi\frac{f_s - f_1}{2}x\right)$, as shown in Fig. 34c, with the frequency $\frac{f_s - f_1}{2}$, which is smaller than either scanning or lattice frequency. It is worth noting that this model is purely based on geometric consideration of the scan and specimen lattice only, and does not affect the physical process of electron–sample interaction. Accordingly, the interference HAADF image still is a Z-contrast image.

One advantage of the SMF method is that it can be used for observation at a lower magnification and in some cases atomic lattice can also be imaged, as shown in Figs. 33c and 35a, a HAADF image of interface of $Ba_{0.3}Sr_{0.7}TiO_3$ (BST) and $SrTiO_3$ (STO) along the ⟨100⟩ zone axis of STO. At such lower magnifications, the specimen suffers less damage from beam irradiation, and also less carbon contamination is produced, both of which are challenging issues in acquiring high-quality STEM images at high magnification especially for beam-sensitive samples.

One can also use SMF to observe dislocations at coherent interfaces at lower magnification as shown in Fig. 35a with a dislocation-like distortion observed. It was acquired with the scanning direction, x, along the interface. In Fig. 35a, we can even determine the "Burgers vector" of a misfit dislocation, $\boldsymbol{a}[0\bar{1}1]$, at the interface. The HAADF image taken at the same area at a magnification 15 M×, Fig. 35b, clearly verifies the existence of such a dislocation with $\boldsymbol{a}[0\bar{1}1]$ Burgers vector. Therefore, using this method to image dislocations with a large field of view gives the convenience in measuring the intensity of dislocations.

7 Application on Micro-area Analysis

In the above sections, different imaging modes in STEM have been introduced, such as HAADF and ABF, which is suitable to image heavy atoms and light atoms, respectively. Besides these imaging, another important application of STEM is analysis on micro area by combination with other analytical signal as mentioned in Sect. 1, for instance, EELS, EDS and NBD, etc. The spectroscopy imaging will be specifically introduced in Chap. 5. For the completeness, however, in this Section, one example

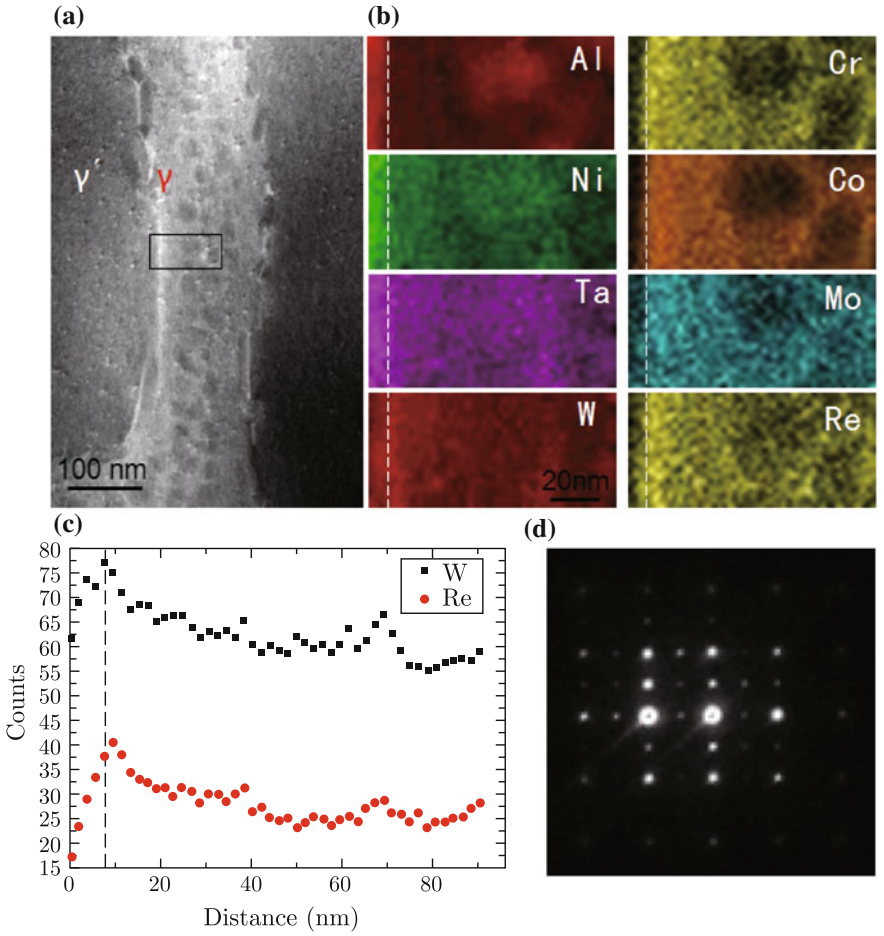

Fig. 36 **a** HAADF image of a nickel-based alloy after the creep test. **b** Element mapping images of major constituents corresponding to areas denoted by a black rectangle in (**a**). **c** Distribution of element Re and W along the direction perpendicular to the interfaces. Dashed lines schematically indicate the γ/γ' interfaces. **d** Diffraction pattern corresponding to the low-contrast area in γ phases in (**a**)

is still given as to the combination between STEM and the analytical methods, EDS and NBD, to achieve the compositional and structural information of the micro area.

Figure 36 shows a HAADF image of a nickel-based alloy after creep test. Comparing with the image of the as-cast alloy as shown in Fig. 12, variations in image contrast can be observed in the γ phase and the γ'/γ' interface shows brighter contrast. To study the redistribution of the major constituents during the creep tests, combination of STEM and EDS are used to analyze the area denoted by a black rectangle in Fig. 36a. From element mapping images as shown in Fig. 36b, enrichment was found as to Cr, Co, Mo, W and Re, γ forming elements, in the γ phase adjacent to the γ/γ' interface. And among heavy elements W and Re were obviously enriched, which can be clearly seen in their distributions along the direction perpendicular to the interface, shown in Fig. 36c. That is why interface shows brighter contrast than other area in Fig. 36a. Moreover, in the area of γ phases with low contrast in Fig. 36a few W and Re as well as Cr, Co and Mo has been found but more Al, Ni and Ta, γ' forming elements, instead. It suggests that these areas may change into γ' phases from γ phases due to the element redistribution during the creep test. To prove this hypothesis two ways can be used, atomic resolution HAADF imaging like Fig. 12 and NBD. Diffraction patterns can be recorded by the axial CCD camera simultaneously with HAADF imaging and EDS collection. One pixel in the HAADF image or EDS mapping corresponds to one diffraction pattern. The NBD pattern corresponding to the area of γ phases with low contrast is shown in Fig. 36d. Ordered γ' phase is identified, which confirms the results of EDS mapping.

8 Discussion and Conclusion

For conventional STEM aberrations of the condenser lens play an important role in determining the point spread of the probe and thus limit the resolution. The invention of the aberration corrector in the end of last century, however, increased the resolution greatly, and in the present equipped with double aberration-correctors, the TEAM 0.5 microscope is capable of producing images with 50 pm resolution (http://ncem.lbl.gov/TEAM-project/index.html). Thus, resolution may not be a problem concerned by electron microscopist anymore. But on the other hand, several factors as mentioned in this chapter, such as channeling effect, Debye-Waller factor and focus, et al. influence the HAADF image contrast and make it deviation from the Z-contrast dependence, especially in aberration-corrected microscopes. Therefore, to fully understand the image contrast and obtain the quantative results, the HAADF image simulations are required, contrary to common perception that HAADF-STEM images are intuitively interpretable in terms of the atomic numbers.

References

Anstis, G.R., Cai, D.Q., Cockayne, D.J.H.: Limitations on the s-state approach to the interpretation of sub-angstrom resolution electron microscope images and microanalysis. Ultramicroscopy **94**, 309–327 (2003)

Ardenne, M.V.: Das Elektronen-rastermikroskop, theoretische grundlagen. ZPhys **109**, 553–572 (1938a)

Ardenne, M.V.: Das Elektronen-rastermikroskop. Praktische Ausführung. Z. Tech. Phys. **19**, 407–416 (1938b)

Blavette, D., Cadel, E., Deconihout, B.: The role of the atom probe in the study of nickel-based superalloys. Mater. Charact. **44**, 133–157 (2000)

Blom, D.A.: Multislice frozen phonon high angle annular dark-field image simulation study of Mo-V-Nb-Te-O complex oxidation catalyst "M1". Ultramicroscopy **112**, 69–75 (2012)

Borisevich, A.Y., Lupini, A.R., Pennycook, S.J.: Depth sectioning with the aberration-corrected scanning transmission electron microscope. Proc. Natl. Acad. Sci. USA **103**, 3044–3048 (2006)

Born, M., Wolf, E.: Principles of Optics. Pergamon Press, Oxford (1980)

Chu, M.W., Liou, S.C., Chang, C.P., Choa, F.S., Chen, C.H.: Emergent chemical mapping at atomic-column resolution by energy-dispersive X-ray spectroscopy in an aberration-corrected electron microscope. Phys. Rev. Lett. **104**, 196101 (2010)

Cowley, J.M.: Image contrast in a transmission scanning electron microscope. ApPhL **15**, 58–59 (1969)

Cowley, J.M.: Electron diffraction phenomena observed with a high resolution STEM instrument. JEMT **3**, 25–44 (1986)

Crewe, A.V.: Scanning electron microscopes-is high resolution possible. Science **154**, 729 (1966)

Crewe, A.V.: High resolution scanning microscopy of biological specimens. Philos. Trans. R. Soc. Lond. Ser. B Biol. Sci. **261**, 61 (1971)

Crewe, A.V., Salzman, D.B.: On the optimum resolution for a corrected stem. Ultramicroscopy **9**, 373–377 (1982)

Crewe, A.V., Wall, J.: A Scanning microscope with 5 a resolution. JMBio **48**, 375 (1970)

Crewe, A.V., Isaacson, M., Johnson, D.: Electron energy loss spectra of nucleic acid bases. Nature **231**, 262 (1971)

Crewe, A.V., Wall, J., Langmore, J.: Visibility of single atoms. Science **168**, 1338 (1970)

Crewe, A.V., Wall, J., Welter, L.M.: A high-resolution scanning transmission electron microscope. JAP **39**, 5861–5868 (1968)

D'Alfonso, A.J., Freitag, B., Klenov, D., Allen, L.J.: Atomic-resolution chemical mapping using energy-dispersive X-ray spectroscopy. Phys. Rev. B **81**, 100101 (2010)

Egerton, R.F.: Electron Energy-Loss Spectroscopy in the Electron Microscope, 3rd edn. Springer (2011)

Engel, A., Wiggins, J.W., Woodruff, D.C.: Comparison of calculated images generated by 6 modes of transmission electron-microscopy. JAP **45**, 2739–2747 (1974)

Erni, R.: Aberration-Corrected Imaging in Transmission Electron Microscopy: An Introduction. ICP/Imperial College Press, London (2010)

Findlay, S.D., Shibata, N., Ikuhara, Y.: What atomic resolution annular dark field imaging can tell us about gold nanoparticles on TiO2TiO2 (110). Ultramicroscopy **109**, 1435–1446 (2009a)

Findlay, S.D., Shibata, N., Sawada, H., Okunishi, E., Kondo, Y., Yamamoto, T., Ikuhara, Y.: Robust atomic resolution imaging of light elements using scanning transmission electron microscopy. ApPhL **95**, 191913 (2009b)

Findlay, S.D., Shibata, N., Sawada, H., Okunishi, E., Kondo, Y., Ikuhara, Y.: Dynamics of annular bright field imaging in scanning transmission electron microscopy. Ultramicroscopy **110**, 903–923 (2010)

Fultz, B., Howe, J.M.: Transmission Electron Microscopy and Diffractometry of Materials, 3rd edn. Springer, New York (2008)

Ge, B.H., Luo, Y.S., Li, J.R., Zhu, J.: Distribution of rhenium in a single crystal nickel-based superalloy. Scr. Mater. **63**, 969–972 (2010)
Ge, B., Luo, Y., Li, J., Zhu, J.: Study of γ/γ' interfaces in nickel-based single-crystal superalloys by scanning transmission electron microscopy. Metall. Mater. Trans. A **42**, 548–552 (2011)
Ge, B., Luo, Y., Li, J., Zhu, J., Tang, D., Gui, Z.: Study of γ/γ' interfacial width in a nickel-based superalloy by scanning transmission electron microscopy. PMagL **92**, 541–546 (2012)
Gu, L., Zhu, C., Li, H., Yu, Y., Li, C., Tsukimoto, S., Maier, J., Ikuhara, Y.: Direct observation of lithium staging in partially delithiated $LiFePO_4$ at atomic resolution. J. Am. Chem. Soc. **133**, 4661–4663 (2011)
Hanssen, K.J.: Contrast transfer of electron-microscope with partial coherent illumination: A ring condensor. Optik **33**, 166–181 (1971)
Haruta, M., Kurata, H., Komatsu, H., Shimakawa, Y., Isoda, S.: Effects of electron channeling in HAADF-STEM intensity in La_2CuSnO_6. Ultramicroscopy **109**, 361–367 (2009)
Howie, A.: Diffraction channelling of fast electrons and positrons in crystals. PMag **14**, 223–237 (1966)
Inada, H., Su, D., Egerton, R.F., Konno, M., Wu, L., Ciston, J., Wall, J., Zhu, Y.: Atomic imaging using secondary electrons in a scanning transmission electron microscope: experimental observations and possible mechanisms. Ultramicroscopy (2010)
Ishizuka, K.: A practical approach for STEM image simulation based on the FFT multislice method. Ultramicroscopy **90**, 71–83 (2002)
Ishikawa, R., Okunishi, E., Sawada, H., Kondo, Y., Hosokawa, F., Abe, E.: Direct imaging of hydrogen-atom columns in a crystal by annular bright-field electron microscopy. Nat. Mater. **10**, 278–281 (2011)
James, E.M., Browning, N.D.: Practical aspects of atomic resolution imaging and analysis in STEM. Ultramicroscopy **78**, 125–139 (1999)
Jia, C.L., Thus, A., Urban, K.: Atomic-scale analysis of the oxygen configuration at a $SrTiO_3$ dislocation core. Phys. Rev. Lett. **95** (2005)
Jia, C.L., Urban, K.: Atomic-resolution measurement of oxygen concentration in oxide materials. Science **303**, 2001–2004 (2004)
Kimoto, K., Asaka, T., Nagai, T., Saito, M., Matsui, Y., Ishizuka, K.: Element-selective imaging of atomic columns in a crystal using STEM and EELS. Nature **450**, 702–704 (2007)
Klenov, D.O., Findlay, S.D., Allen, L.J., Stemmer, S.: Influence of orientation on the contrast of high-angle annular dark-field images of silicon. Phys. Rev. B **76**, 014111 (2007)
Komoda, T.: Electron microscopic observation of crystal lattices on level with atomic dimension. Jpn. J. Appl. Phys. **5**, 603–607 (1966)
LeBeau, J.M., Findlay, S.D., Wang, X., Jacobson, A.J., Allen, L.J., Stemmer, S.: High-angle scattering of fast electrons from crystals containing heavy elements: simulation and experiment. Phys. Rev. B **79**, 214110 (2009)
Lin, J.A., Cowley, J.M.: Calibration of the operating parameters for an HB5 stem instrument. Ultramicroscopy **19**, 31–42 (1986)
Liu, J.: Scanning transmission electron microscopy of nanoparticles. In: Wang Z. (ed.) Characterization of nanophase materials, pp. 81–132 (2000)
Mathews, W.W.: The use of hollow-cone illumination for increasing image contrast in microscopy. Trans. Am. Microsc. Soc. **42**, 190–195 (1953)
Misell, D.L., Stroke, G.W., Halioua, M.: Coherent and incoherent imaging in scan-ning-transmission electron-microscope. J. Phys. D Appl. Phys. **7**, L113–L117 (1974)
Mitome, M., Takayanagi, K., Tanishiro, Y.: Improvement of resolution by convergent-beam illumination in surface profile images of high resolution transmission electron microscopy. Ultramicroscopy **33**, 255–260 (1990)
Mittal, A., Mkhoyan, K.A.: Limits in detecting an individual dopant atom embedded in a crystal. Ultramicroscopy **111**, 1101–1110 (2011)

Muller, D.A., Kourkoutis, L.F., Murfitt, M., Song, J.H., Hwang, H.Y., Silcox, J., Dellby, N., Krivanek, O.L.: Atomic-scale chemical imaging of composition and bonding by aberration-corrected microscopy. Science **319**, 1073–1076 (2008)

Nellist, P.D.: The Principles of STEM Imaging, in: S.J., Pennycook, Nellist P.D. (eds.) Scanning Transmission Electron Microscopy: Imaging and Analysis, pp. 91–116. Springer, New York (2011b)

Nellist, P.D.: The principles of STEM imaging. In: Pennycook, S.J., Nellist P.D. (eds.) Scanning Transmission Electron Microscopy: Imaging and Analysis. p. 92. Springer, New York (2011a)

Nellist, P.D., Rodenburg, J.M.: Beyond the conventional information limit: the relevant coherence function. Ultramicroscopy **54**, 61–74 (1994)

Nellist, P.D., Cosgriff, E.C., Behan, G., Kirkland, A.I.: Imaging modes for scanning confocal electron microscopy in a double aberration-corrected transmission electron microscope. Microsc. Microanal. **14**, 82–88 (2008)

Okunishi, E., Ishikawa, I., Sawada, H., Hosokawa, F., Hori, M., Kondo, Y.: Visualization of light elements at ultrahigh resolution by STEM annular bright field microscopy. Microsc. Microanal. **15**, 164–165 (2009)

Pennycook, S.J.: A scan through the history of STEM. In: Pennycook, S.J., Nellist, P.D. (eds.) Scanning Transmission Electron Microscopy: Imaging and Analysis, pp. 1–90. Springer, New York (2011)

Pennycook, S.J., Jesson, D.E., Chisholm, M.F., Browning, N.D., McGibbon, A.J., McGibbon, M.M.: Z-contrast imaging in the scanning transmission electron microscope. Microsc. Microanal. **1**, 231–251 (1995)

Rose, H.: Phase-contrast in scanning-transmission electron-microscopy. Optik **39**, 416–436 (1974)

Rose, H.: Nonstandard imaging methods in electron-microscopy. Ultramicroscopy **2**, 251–267 (1977)

Su, D., Zhu, Y.M.: Scanning moire fringe imaging by scanning transmission electron microscopy. Ultramicroscopy **110**, 229–233 (2010)

Voyles, P.M., Grazul, J.L., Muller, D.A.: Imaging individual atoms inside crystals with ADF-STEM. Ultramicroscopy **96**, 251–273 (2003)

Yamazaki, T., Kawasaki, M., Watanabe, K., Hashimoto, I., Shiojiri, M.: Artificial bright spots in atomic-resolution high-angle annular dark field STEM images. J. Electron Microsc. **50**, 517–521 (2001)

Yu, Z., Muller, D.A., Silcox, J.: Study of strain fields at a-Si/c-Si interface. J. Appl. Phys. **95**, 3362–3371 (2004)

Yu, Z., Muller, D.A., Silcox, J.: Effects of specimen tilt in ADF-STEM imaging of a-Si/c-Si interfaces. Ultramicroscopy **108**, 494–501 (2008)

Zeitler, E., Thomson, M.G.R.: Scanning transmission electron microscopy 2. Optik **31**, 359 (1970a)

Zeitler, E., Thomson, M.G.R.: Scanning transmission electron microscopy 1. Optik **31**, 258 (1970b)

http://en.wikipedia.org/wiki/Snell's_law

http://ncem.lbl.gov/TEAM-project/index.html